

*FAR ULTRAVIOLET SPECTROSCOPIC EXPLORER SURVEY OF THE LOCAL
INTERSTELLAR MEDIUM WITHIN 200 PARSEC*

N. LEHNER^{1,2}, E.B. JENKINS³, C. GRY^{4,5}, H.W. MOOS¹, P. CHAYER^{1,6}, S. LACOUR¹
Accepted Version

ABSTRACT

We present *Far Ultraviolet Spectroscopic Explorer* observations of the interstellar gas toward 30 white dwarf and 1 subdwarf (SdO) stars. These sightlines probe the Local Bubble (LB) and the local interstellar medium (LISM) near the LB. We systematically measure the column densities for the following species: C II, C II*, C III, N I, N II, O I, Ar I, Si II, P II, Fe II, Fe III, and H₂. Our survey detected only diffuse H₂ molecular clouds ($f_{\text{H}_2} \lesssim 10^{-4}$) along six sightlines. There is no evidence from this study that H₂ exists well inside the perimeter of the LB. The kinematical temperature for H₂ is less than the usual temperature observed in the local interstellar clouds, implying different gas phases in the LISM. The relative abundance ratios of Si II, P II, and Fe II give insight about the dust content. These ratios vary, but are similar to the depletion patterns observed in warm and halo diffuse clouds in more distant sightlines in the Galaxy. The N I/O I and Ar I/O I ratios are significantly subsolar within the LB. Outside the LB a larger scatter is observed from subsolar to solar. Because Ar and N are only weakly depleted into dust grains if at all, the deficiencies of their neutral forms are likely due to photoionization. The evidence for significant ionization of N (and hence Ar) is strengthened by the detection and measurement of N II, which is a dominant ion for this element toward many sightlines. C III appears to be ubiquitous in the LISM toward our sightlines, but C II remains the dominant ionization stage of C. The limits on Fe III/Fe II imply that Fe II is the dominant ion. These observations imply that photoionization is the main ionization mechanism in the LISM and do not support the existence of a highly ionized condition in the past. In view of the variations observed in the different atomic and ionic ratios, the photoionization conditions vary significantly in the LB and the LISM. The cooling rate in the LISM, l_c (in $\text{erg s}^{-1} (\text{H I atom})^{-1}$), derived from the emission of the C II 157.7 μm line has a mean value of $\log l_c = -25.59 \pm 0.32$ dex, very similar to previous determinations.

Subject headings: ISM: clouds – ISM: structure – ISM: atoms – ISM: abundances – ultraviolet: ISM – white dwarfs

1. INTRODUCTION

Because of its proximity, the local interstellar medium (LISM) provides an unique opportunity to study in detail the physics of the warm (partially ionized) interstellar gas. Such gas is a major component of the interstellar material in the Galaxy and in other galaxies. The overall characteristics (temperatures, densities, kinematics) of the LISM were determined with ground-based telescopes and the *Copernicus*, *International Ultraviolet Explorer (IUE)*, the *Hubble Space Telescope (HST)* satellites (e.g., McClintock et al. 1975; Bruhweiler & Kondo 1982; Frisch & York 1983; Linsky et al. 1993; Lallement et al. 1995; Redfield et al. 2002). Measurements of interstellar gas after it has entered the heliosphere has also provided information on the interstellar medium very close to the sun (see, e.g., studies of the local interstellar cloud by Lallement 1998 and by Slavin & Frisch 2002 and references therein).

From the ground-based observations, via mainly the Ca II K and Na I D absorption lines, very accurate absolute wavelength and very high spectral resolution provide precise information on the local gas dynamics and the

complex velocity structure of nearby gas (e.g., Vallerga et al. 1993; Ferlet 1999, and references therein). UV resonance absorption lines are much stronger than the available optical absorption lines (which are not in the dominant ionization stages), and are therefore more sensitive probes of the warm, low density LISM. Major advances in determining the physical conditions have been carried-out with UV observations, especially in the last decade, with the Goddard High Resolution Spectrograph (GHRS) and the Space Telescope Imaging Spectrograph (STIS) onboard *HST* (e.g., Linsky et al. 1993; Lallement et al. 1995; Lallement 1996; Linsky 1996).

With high spectral resolution ultraviolet observations, the physical properties of the cloud surrounding our solar system (the local interstellar cloud, LIC) can be estimated. The LIC is not very dense ($n_{\text{H}} \sim 0.1 \text{ cm}^{-3}$), but it is warm ($T \sim 7000 \text{ K}$) and partially ionized (e.g., Frisch & York 1983; Lallement 1996; Linsky 1996). Near the LIC, there are similar clouds with different velocities (see, Linsky et al. 2000). All these clouds constitute collectively the LISM, and the clouds within roughly 100 pc are in a region called the Local Bubble (LB; the cavity has a radius

¹ Department of Physics and Astronomy, The Johns Hopkins University, Bloomberg Center, 3400 N. Charles Street, Baltimore, MD 21218.

² Current address: Department of Astronomy, University of Wisconsin, 475 North Charter Street, Madison, WI 53706. nl@astro.wisc.edu

³ Princeton University Observatory, Princeton, NJ 08544.

⁴ ISO Data Center, ESA, Villafranca del Castillo, P.O. Box 50727, 28080 Madrid, Spain.

⁵ Laboratoire d'Astronomie Spatiale, B.P. 8, F-13376 Marseille, France.

⁶ Department of Physics and Astronomy, University of Victoria, P.O. Box 3055, Victoria, BC V8W 3P6, Canada.

of about 100 pc in almost every direction, except toward one very low column density direction (β CMa) where it extends to ~ 200 pc; Sfeir et al. 1999). Na I absorption line studies by Sfeir et al. (1999) show that the boundary of the LB is delineated by a sharp gradient in the neutral gas column density with increasing radius. The distance of this boundary deduced from X-ray data is generally smaller by about 30% (see Snowden et al. 1998). In this study, we use the *Far Ultraviolet Spectroscopic Explorer (FUSE)* satellite to survey sightlines with distances less than 200 pc. For the purposes of this study, this distance will define the extent of the LISM. Even though the distances are not great in the LISM, the sightlines are expected usually to have complex kinematical structure (e.g., Lallement et al. 1995).

EUVE observations also have improved our knowledge of the ionization structure of the LISM (see the review by Bowyer, Drake, & Vennes 2000, and references therein). The *EUVE* data show that the neutral helium to neutral hydrogen ratio is about 0.07, which is somewhat less than the cosmic abundance of He to H of 0.1 (Dupuis et al. 1995). Helium is therefore more ionized than H. Also, He shows less variability in its degree of ionization from one region to the next (Wolff, Koester, & Lallement 1999). One possible explanation for the high fractional ionization of He in the LISM is that there has not been enough time for the ionized He to recombine to an equilibrium concentration from a more highly ionized condition in the past, perhaps from the influence of radiation from a supernova or its shockwave less than few 10^6 years ago (Frisch & Slavin 1996; Lyu & Bruhweiler 1996). A different alternative is that the LISM is currently exposed to a strong, steady flux of photons with $E > 24.6$ eV (e.g., a conductive interface between the LISM and a surrounding medium at $T \sim 10^6$ K; Slavin & Frisch 2002, or by recombination radiation from highly ionized but cool gases; Breitschwerdt & Schmutzler 1994). A way to distinguish between these possibilities is to study the lightly depleted elements Ar, N, and O (Sofia & Jenkins 1998). In particular, the ionization of Ar (and to a lesser extent of N) can help us to differentiate between photoionization equilibrium and non-equilibrium cooling models.

It is possible to increase our knowledge of the ionization structure of the LISM significantly by using data from *FUSE* (Jenkins et al. 2000; Lehner et al. 2002; Moos et al. 2002; Wood et al. 2002b). For instance, Jenkins et al. (2000) found a deficiency of Ar I toward 4 white dwarf (WD) stars, thus favoring photoionization equilibrium. In the present work, we increase the sample to 31 stars that are located within 200 pc. WDs are particularly good background objects for studying the LISM because they are nearby, they have relatively simple stellar continua, and they are often nearly featureless. *FUSE* gives access to the wavelength interval between 905 Å and 1187 Å, a region containing features of some important neutral species (N I, O I, and Ar I), many ionized species (C II, C III, N II, P II, Fe II, and Fe III), and H₂. Surveys of O VI interstellar absorption and D I/O I ratio will be discussed by Oegerle et al. (2003) and Hébrard et al. (2003), respectively. Although *FUSE* has a moderate resolution of $R \sim 20,000$ and, hence, only the properties of the dominant cloud or the “average” properties of the clouds can be derived, the

large number of resonance lines for atoms in several ionization stages as well as molecular lines provides the unique opportunity to study in detail the ionization structure, dust, and molecules in the LISM.

2. OBSERVATIONS

2.1. *The Sample*

In Table 1, we list the positions, spectral types, distances, and heliocentric velocities for the sample of 31 stars observed with *FUSE*. The distribution of the targets on the sky is shown in Galactic coordinates in Figure 1. There is a good coverage of the sky in almost each quadrant with the exception of the region spanned by $l = 180^\circ - 360^\circ$ and $b \geq 0^\circ$. Most of the WDs are from the *FUSE* PI Team programs (P104 and P204) used to study D/H and O VI in the LISM. The primary criterion for selecting the stars in Table 1 was that we would be able to measure the species of interest for this work (see § 3) with a sufficient degree of confidence.

Recently, in the course of the *FUSE* observatory program “Survey of White Dwarfs from the McCook and Sion Survey” (Z903), several other WDs were observed. The quality of these data are not good enough for this study because strong airglow emission lines are present at all wavelengths and the signal-to-noise levels are too low (the flux of these WDs in this program are systematically lower than in the PI team programs). We also note that these targets do not fill in the deficiency of targets in the quadrant at $l = 180^\circ - 360^\circ$, $b \geq 0^\circ$.

2.2. *Instrument and data reduction*

The *FUSE* instrument consists of four channels: two optimized for the short wavelengths (SiC 1 and SiC 2; 905–1100 Å) and two optimized for longer wavelengths (LiF 1 and LiF 2; 1000–1187 Å). There is, however, overlap between the different channels, and, generally, a transition appears in at least two different channels. More complete descriptions of the design and performance of the *FUSE* spectrograph are given by Moos et al. (2000) and Sahnou et al. (2000). To maintain optimal spectral resolution the individual channels were not co-added together. Also, measurements on the independent spectra could be compared with each other to obtain information about the effects of detector fixed pattern noise. Detailed information for each sightline, including whether the low resolution (LWRS) apertures or the medium resolution (MDRS) apertures were used, can be found in Table 1.

Standard processing with the current version of the calibration pipeline software (version 2.0.5 and higher) was used to extract and calibrate the spectra. The software screened the data for valid photon events, removed burst events, corrected for geometrical distortions, spectral motions, satellite orbital motions, and detector background noise, and finally applied flux and wavelength calibrations. The extracted spectra associated with the separate exposures were aligned by cross-correlating the positions of absorption lines, and then co-added. In some cases, the lack of strong absorption lines or the contamination of airglow lines prevented us from determining the relative displacements, so we simply coadded the spectra with no shifts. Generally, the different exposures were obtained successively, so no large shifts were expected and no significant

loss of spectral resolution was observed. The co-added spectra were finally rebinned by 4 pixels (~ 27 mÅ) since the extracted data are oversampled.

Figure 2 presents two examples of *FUSE* calibrated spectra of WDs. As can be seen in the figure, the stellar continua are relatively simple and can be fitted with low-order (≤ 3) Legendre polynomials. The primary error sources are statistical noise, fixed-pattern noise, and possible saturation effects in the lines. The fixed-pattern noise is reduced by comparing the same spectral feature in different channels, while saturation can be examined when there are several transitions of the same species with different $f\lambda$ values (§ 3).

3. SPECTRAL FEATURES

3.1. General Considerations

The primary objective of this work is to measure the column densities of the neutral atoms, weakly ionized atoms and molecular hydrogen toward sightlines within ~ 200 pc in order to probe the physical conditions within the LISM. For such study *FUSE* provides access to several important resonance lines, and we have measured systematically the column densities, N , (or limits on the column densities) for the following species: C II, C II*, C III, O I, N I, N II, Si II, P II, Ar I, Fe II, and Fe III. The column densities of H₂ were determined by using the Lyman and Werner bands. We note that P III and N III also are present in the *FUSE* bandpass and are potentially interesting ions. However, the P III transition is too weak to be detected and its 3σ upper limit does not constrain the ratio P II/P III in a meaningful way. N III is blended with the saturated Si II line and possibly with photospheric N III making any measurements of this line highly uncertain. However, upper limits obtained by assuming that N III is not blended and lies on the linear part of the curve of growth (COG) show that N III is not the dominant ion stage of N in the LISM. Corrections for saturation would increase the upper limit, but this effect is likely less than the contribution from the Si II blend. Therefore, nitrogen is primarily N I and N II in the LISM.

In Table 2, we summarize the atomic/ionic transitions used in this work. To measure the column densities (see below), we adopted wavelengths and oscillator strengths from the Morton (2000, private communication) atomic data compilation. This compilation is similar to the Morton (1991) compilation with only a few minor updates to the atomic parameters for lines of interest in this study. For the Fe II lines, the new oscillator strengths derived by Howk et al. (2000) were adopted. We note, however, that there is a new laboratory measurement of the f -value for Fe II $\lambda 1144.9$ ($f = 0.083 \pm 0.006$, Wiese, Bonvallet, & Lawler 2002), which is about 30% lower than the experimental value of Howk et al. (2000). However, Wiese, Bonvallet, & Lawler (2002) note that additional study is necessary for the other transitions available in the *FUSE* bandpass, rather than a simple rescaling, as they are further down on the COG than the Fe II $\lambda 1144.9$ line. As we use all the transitions available in the *FUSE* spectrum, we employ the f -values of Howk et al. (2000).

For molecular hydrogen, we use the wavelengths from Abgrall et al. (1993a,b). The H₂ f -values were calculated from the emission probabilities given by those authors.

3.2. Photospheric Lines

To varying degrees, WD stars have sharp metal photospheric lines that can mimic interstellar lines, and therefore it is important to identify and disentangle them. Some WDs can be pure hydrogen (no photospheric metal lines) and some have only small amounts of metals in their photosphere. Their metallicity is generally very sub-solar (less than a few 10^{-3} solar metallicity, Z_{\odot}), and only a few metal-rich WDs are as high as $0.1 Z_{\odot}$ (e.g., WD 2211–495, WD 0621–376). As a consequence, WDs have relatively smooth continua with only a few stellar lines. Figure 2 presents spectra of two WDs, one pure hydrogen and the other with some metals, with the interstellar lines flagged. Table 1 summarizes the metallicity of the WDs.

The lines that can be affected by photospheric lines are C III $\lambda 977$, Ar I $\lambda 1066$, P II $\lambda 1052$, and Fe III $\lambda 1122$. C III can be present in WDs with $20 \times 10^3 \lesssim T_{\text{eff}} \lesssim 50 \times 10^3$ K, and peak at $\sim 30 \times 10^3$ K (see Chayer, Fontaine, & Wesemael 1995). Thus, when the star is not pure hydrogen, some contamination is expected for C III. Generally the stellar radial velocity is not different enough from the interstellar component to be able to distinguish between the two components. Photospheric Fe III can be also present for WDs with $T_{\text{eff}} \lesssim 40 \times 10^3$ K. Moreover, Fe III $\lambda 1122.53$ is blended with photospheric Si IV $\lambda 1122.49$. For this species, we have a direct diagnostic for knowing if there is photospheric Si IV $\lambda 1122$ or Fe III $\lambda 1122$ by inspecting the lines Si IV $\lambda 1128$ and Fe III $\lambda 1128$ (see Figure 2 in Chayer et al. 2000). P II and Ar I are not found in the photosphere of the WDs, but can be blended with Fe VI, Ni VI $\lambda 1152$ and Si IV $\lambda 1066$, respectively. Fe VI (and Ni VI) are present in significant quantities only at $T_{\text{eff}} \gtrsim 60 \times 10^3$ K (Chayer, Fontaine, & Wesemael 1995). Therefore for most of our sample, these blends with Fe VI and Ni VI are not much of a concern. For Si IV $\lambda 1066$ we look at longer wavelengths (e.g. Si IV $\lambda 1128$) for possible presence of this line. We finally note that some of the N I, O I, Fe II, and H₂ transitions may be blended with some stellar lines, but the (generally) large numbers of transitions for these species allow us to detect if a specific line is contaminated.

3.3. Circumstellar Lines

Our survey used hot WDs, typically with temperatures ranging from 30,000 to 70,000 K (the subdwarf SdO BD+28°4211 has a temperature of 82,000 K; Sonneborn et al. 2002). Such hot WDs are emitting a large number of ionizing ultraviolet photons, creating Strömgren spheres with radii from 8 upto 30 pc depending on the electron density and the temperature of the WD (Dupree & Raymond 1983; Tat & Terzian 1999). Bannister et al. (2003) recently found direct evidences of such circumstellar absorption features (in form of high ions such as C IV) in the spectra of 4 WDs out of 11 present in our survey. Therefore, our study of the ionization conditions in the LISM could *a priori* be systematically biased because of the use of hot WDs. However, to probe these conditions, we employ mainly diagnostics from neutral species, such as N I, O I, and Ar I, species not present in the completely ionized Strömgren spheres. We have found no correlation between the ratios of Ar I/O I and N I/O I with the temperature of the WDs. While it is clear that the hot WDs

participate to the overall ionization of the LISM (Vallerga 1998; Slavin & Frisch 2002), we have no evidence that stronger EUV sources give different results compared to weaker EUV sources in our column density ratios.

3.4. Geocoronal Emission Lines

Contamination of the spectra by geocoronal emission can be significant for the LWRs apertures of the *FUSE* spectrograph. Such emission lines are very strong at H I Ly β , but decline rapidly in strength for the higher Lyman lines. During the sunlit part of the orbit, airglow emission lines are also present for many of the same lines of N I, O I, and Ar I used to measure the absorption by interstellar species. The importance of airglow emissions depends on many factors, including the fraction of sunlit time, the limb angle, the flux of the target, the aperture used, and the length of individual exposures. For the stars considered in this study, the observational strategy was to reduce the contribution from airglow lines: (1) The targets were observed in a manner that maximized the night time fraction, ranging typically from 30% to 100% (only WD 1234+481 was observed with basically no night time). (2) In order to remove small spectral shifts during an observation caused by thermally induced motion of the optics, an exposure is broken up into a large number of sub-exposures. Correlation techniques using uncontaminated interstellar lines are used to remove the shifts between the spectra and they are then added. To the extent the shifts are due to telescope mirror motions rather than grating motions, these shifts will smear out the airglow contribution. In practice, impact of the airglow contamination is reduced by this technique. (3) The objects studied are relatively bright with fluxes from a few 10^{-12} to 10^{-11} erg cm $^{-2}$ s $^{-1}$ Å $^{-1}$. (In contrast the stars from the Z903 program have lower fluxes, long individual exposure times, and are observed largely in day time.) However, even under the conditions mentioned above, the airglow could still be significant. Therefore, we took several steps discussed below to check for possible contamination.

The widths of the airglow lines are determined by the size of the spectrograph apertures. For the LWRs aperture, the width of an airglow is typically 0.35 Å, while it is typically 0.045 Å for the MDRS aperture. Figure 2 illustrates the differences in strength and width of the airglow lines between the MDRS aperture (WD 1800+685, night fraction of 0.85) and LWRs aperture (WD 0131–163, night fraction of 0.95). Hence with the LWRs aperture, the primary concern for measuring the interstellar lines considered here is the continuum placement, but for the MDRS aperture, the width is small enough that the emission could fill the interstellar lines. Several of our targets were observed with both the LWRs and MDRS apertures. The column densities generally agree within the errors, and in particular there was no systematic smaller column densities derived with the MDRS compared to those derived with the LWRs.

Feldman et al. (2001) have reported the brightnesses of the terrestrial day airglow lines using the *FUSE* instrument. We have examined airglow lines not blended with interstellar lines to estimate if our interstellar measurements could suffer from airglow contamination. At $\lambda > 1080$ Å, we use the O I $^1D-^1D^0$ $\lambda 1152$ line as an indi-

cator for the presence of N I emission near 1134 Å, since the lines have comparable strengths. This airglow line can cause a continuum placement problem for the measurement of P II $\lambda 1152$ as shown in Figure 2 in the spectrum of WD 0131–163. We were careful to use the N I $\lambda 1134$ lines only when these lines were not contaminated by airglow. At $1000 < \lambda < 1080$ Å, we checked the strengths of several O I airglow lines at 1027, 1028 and 1042 Å. These lines have strengths that indicate the strengths of the O I $\lambda 1039$ and Ar I $\lambda\lambda 1048, 1066$ airglow lines. We do not find any cases where the contamination could be troublesome (in any case the 1σ errors quoted here should be larger than the effects of contamination). Finally, at $\lambda < 1000$ Å, where the most useful lines of N I and O I are located, the airglow emissions are negligible based on O I $\lambda 990$. Generally, we are confident that the airglow lines do not seriously compromise our interstellar measurements in ways we do not recognize.

3.5. Interstellar Absorption Lines

3.5.1. Species with Only One or Two Transitions

The apparent optical depth (AOD) method (Savage & Sembach 1991) was used when only one or two lines of the same atomic species were available. The absorption profiles were converted into apparent optical depths per unit velocity, $\tau_a(v) = \ln[I_c/I_{\text{obs}}(v)]$, where I_c , I_{obs} are the intensity without and with the absorption, respectively. $\tau_a(v)$ is related to the apparent column density per unit velocity, $N_a(v)$ (cm $^{-2}$ (km s $^{-1}$) $^{-1}$) through the relation $N_a(v) = 3.768 \times 10^{14} \tau_a(v) / [f \lambda (\text{Å})]$. The integrated apparent column density is equivalent to the true integrated column density in cases where the absorption is weak ($\tau \lesssim 1$) or the lines are resolved. This method was also used to place a lower limit on a saturated line.

For C II and N II, only a strong transition is available, and therefore, except for a few cases, the column densities are lower limits. The P II transition is weak for all of the sightlines considered. C II* is also usually relatively weak for the sightlines considered, but can be slightly blended with the Lyman 5–0 R(1) line of H $_2$. When hydrogen molecules are present along a sightline, the contribution of both lines can still be measured because the shift between the two lines is large enough.

Si II has two transitions. The weakest one is free of blending with other interstellar or stellar lines, but the strongest transition at 989.873 Å is usually saturated and blended with N III of interstellar or stellar origin.

For Ar I, two transitions are also available at 1048.22 and 1066.66 Å, with the latter being the weakest transition of the two. We can therefore check for the effect of saturation, except when the WD is not pure hydrogen in which case Ar I $\lambda 1066.66$ is blended with the stellar Si IV $\lambda 1066.66$.

3.5.2. Species with several (> 2) transitions: N I, O I, Fe II, and H $_2$

A COG analysis was undertaken when several lines were present (N I, O I, Fe II, and H $_2$) by using the measured equivalent widths. The equivalent widths were measured by directly integrating the intensity, and their errors were derived following the method described by Sembach & Savage (1992). A single component Gaussian (Maxwellian)

curve of growth was constructed in which the Doppler parameter b and the column density were varied to minimize the χ^2 between the observed equivalent widths and a model curve of growth. For H_2 , first a COG was constructed for the set of lines within each rotational level ($J = 0, \dots, 3$). The resulting column densities and b -values were then used as the starting point for a χ^2 minimization of a COG that simultaneously included all of the rotational levels with the column density for each level and a single b value as free parameters.

Depending on the quality of the data and the amount of matter along a given sightline, we found that generally the column densities of N I, O I, and Fe II were well determined with a COG because they have several transitions with different $f\lambda$ in the *FUSE* bandpass. We found that fixed-pattern noise was not a serious problem, and the effects of saturation can be reasonably well understood. In Table 3, we compare the b -values of N I and O I obtained from the COG analysis, and within the errors, they are generally similar. In isolated cases where there was no good constraint on b , we used the b -value from one species to constrain the column density of the other. Those cases are indicated by colons in Table 3. The different Fe II transitions generally lie on the linear part of the COG.

Even though we considered seriously the saturation problem, with the *FUSE* spectral resolution, it still could be that narrow, unresolved components could be concealed by broader features. Jenkins (1986) showed, however, that column densities remain accurate to $\sim 10\%$ provided that the lines are not heavily saturated (central optical depth such as $\tau_0 < 2$) and b and τ do not have a bimodal distribution function. Three sightlines (WD 0501+527, WD 1254+223, and WD 1314+293) of our sample were obtained with high spectral resolution using STIS. Redfield & Linsky (2003), but see also Vidal-Madjar et al. (1998) and Kruk et al. (2002), derived the column densities of several species considered in our survey for these sightlines, and their total column density measurements are in agreement within 1σ with ours. This shows that *FUSE* measurements are reliable despite the moderate spectral resolution of the instrument. It also shows that the oscillator strengths of the species available in the *FUSE* wavelengths are also reliable.

3.5.3. 3σ Upper Limits

The 3σ upper limits for the equivalent widths are defined as $W_{\min} = 3\sigma \delta\lambda$, where σ is the inverse of the continuum S/N ratio per resolution element $\delta\lambda = 0.1 \text{ \AA}$ FWHM. The corresponding 3σ upper limits on the column density, presented in Table 4, are obtained from the corresponding equivalent width limits and the assumption of a linear curve of growth.

3.6. Results from Other Sources

Table 1 lists the sources of the column densities when they were derived from other investigations. For the sightlines that are reported in the ApJS special issue on the determination of D/H with *FUSE* (Hébrard et al. 2003; Kruk et al. 2002; Lehner et al. 2002; Lemoine et al. 2002; Sonneborn et al. 2002; Wood et al. 2002a), we complemented the measurements with additional measurements of the column densities for species considered here but

not in those papers. In addition, for WD 1631+781 and WD 2004-605, the values reported here are a mean between our methods (AOD and COG) and the profile fitting method reported by Hébrard et al. (2003). We note that our values agreed at $1 - 2\sigma$ level. For WD 1211+332, WD 2247+583, WD 2309+105, and WD 2331-475, the column densities are from Oliveira et al. (2003). For WD 0004+330, they are from Oliveira et al. (private communication, 2003). They were also obtained using several independent methods. In addition, we made independent measurements of the column species for WD 0004+330 and WD 2331-475; our values agreed at the $1 - 2\sigma$ level.

The column density results are summarized for each sightline in Table 4 for the atomic species and in Table 5 for the molecular hydrogen. All the errors (except upper limits) are 1σ .

Table 5 also lists the rotational excitation temperature of H_2 for each sightline. A single straight line with a slope characterized by T_{ex} fits all the observed levels $J = 0, \dots, 3$, except toward WD 0004+330 (see § 5). No rotational level higher than $J = 3$ was detected.

4. GENERAL FINDINGS

4.1. Sky-Distribution of the O I Column Density

O I is an excellent tracer of H I because its ionization potential and charge exchange reactions with hydrogen ensure that the ionization of H I and O I are strongly coupled. Only a few sightlines considered in this work have an accurate H I column density measurement (see Moos et al. 2002). Measuring H I column densities is particularly complex for LISM sightlines because the H I Lyman series transitions in the *FUSE* wavelength range are generally on the flat part of the COG. In addition, the interstellar lines are narrow enough that blending with the stellar spectra can be a significant source of uncertainty. Therefore, we use O I as a proxy of H I, adopting the O I/H I ratio derived by Oliveira et al. (2003) (who considered one sightline plus the sightlines in Moos et al. 2002), $\text{O I/H I} = (3.17 \pm 0.19) \times 10^{-4}$, to estimate the amount of H I along a given sightline. This ratio is similar to values obtained for more distant sightlines ($\text{O I/H I} = (3.43 \pm 0.15) \times 10^{-4}$; $\text{O I/H I} = (4.08 \pm 0.14) \times 10^{-4}$; Meyer, Cardelli, & Sofia 1997; André et al. 2003a, respectively), showing that O is usually a good proxy for H in different environments of the Galaxy. Also O is the most abundant species after H and He, making it a general good tracer of neutral gas over a large range of values of column density. The O I/H I ratio may vary in regions of elevated dust and density (Cartledge et al. 2001) or possibly in regions where the signature of stellar processed gas is still visible (Hoopes et al. 2003), but these conditions likely do not hold for the sightlines studied here. Therefore, we expect O I to be a reliable proxy for H I in this study.

Figure 1 shows the distribution of the O I column density (and thus H I) in the Galactic sky. The diameter of each circle is inversely proportional to the WD's distance and the intensity of the shading of the symbol indicates the total column density along a given line of sight. Because the clouds are not resolved (see below), most of the sightlines have column densities between 15.5 and 16.5 dex. Generally, the farthest sightlines result in the largest column densities. However, there are cases where, for ex-

ample at $-90^\circ \leq b \leq 0^\circ$ and $300^\circ \lesssim l \lesssim 360^\circ$, sightlines with very different stellar distances (stellar distances being only an *upper* limit on the distances of the interstellar clouds) have a similar column density. At $d < 100$ pc, the North Galactic pole sightlines seem to have much lower column densities than those near the South Galactic pole (see also, Génova et al. 1990; Redfield et al. 2002; Welsh et al. 1999). The lowest column density is found near $l \sim 190^\circ$ (WD 0549+158) which is known for its relatively low density (Gry & Jenkins 2001; Redfield et al. 2002).

4.2. Sightlines and the Local Bubble

A typical sightline goes through the Local Interstellar Cloud (LIC), other warm partially ionized clouds, the Local Bubble (LB), and, depending on the distance of the star, might even go beyond the LB. With very high resolution observations ($R > 10^5$ – 10^6), the different clouds along a given sightline can be resolved as long as they do not occur at the same velocity. However, with *FUSE*, a resolution of only about 20 km s^{-1} is achieved. As a result, the column densities derived in this study reflect the total amount of matter along a given line of sight.

Sfeir et al. (1999) have used the absorption line studies of Na I D, a tracer of cold neutral gas, to map the boundary of the LB. The LB consists of an interstellar cavity of low density neutral gas with radii between 65–250 pc in the galactic plane and ~ 100 pc in other directions which is surrounded by a denser neutral gas boundary (also referred as the “wall”). The H I density corresponding to the wall is about 19.3 dex (20 mÅ equivalent width for Na I D). Therefore both the distance and total H I column density are used as a guide on whether or not a sightline extends beyond the edge of the LB.

Based on these arguments, the clouds toward the following targets should be well inside the LB ($\log N(\text{H I}) < 19.0$ dex): WD 0050–332, WD 0455–282, WD 0501+527, WD 0549+158, WD 0621–376, WD 1254+223, WD 1314+293, WD 1634–573, WD 2111+498, WD 2152–548, WD 2211–495, and WD 2331–475. In contrast, the following sightlines have $19.0 \lesssim \log N(\text{H I}) \lesssim 19.3$ dex and therefore must be close to the boundary: WD 1211+332, WD 1615–154, WD 1636+351, WD 2004–605, and WD 2309+105. All the other sightlines have $\log N(\text{H I}) > 19.3$ dex, though we note that some of them have values close to the approximate boundary. In short, some of our sightlines are well inside the LB, some are very close to the wall, and some are beyond. We note that the column densities in the LIC are of the order of 5×10^{16} – $2 \times 10^{18} \text{ cm}^{-2}$ (Redfield & Linsky 2000). Therefore material in the LIC generally constitutes only a very small fraction of an observed total column density.

We emphasize again that even though some of the sightlines reside completely within the LB, it is likely that several clouds separated by less than 20 km s^{-1} are present along a given sightline. Therefore, with the *FUSE* observations we only derive either the properties of the dominant (larger column density) cloud or a mixture of these clouds properties. This is the case, for example, for G191–B2B and GD 246 where 2 or 3 clouds are detected using higher spectral resolution (Vidal-Madjar et al. 1998; Oliveira et al. 2003). This hidden component structure can subsequently complicate the physical interpretation of

these spectra (see § 6 and 7).

4.3. Distribution of the Column Densities for the Different Species

In Figure 3, we present the column density distribution of O I, N I, Ar I, Si II, Fe II, and P II (based only on the measurements – not the limits – presented in Table 4). Recently, Redfield et al. (2002) presented the column density distribution of *individual* clouds along sightlines within 100 pc. A comparison with the distribution of Fe II column density in their work (their Figure 9) and this work clearly shows an increase in our sample of ~ 1 dex in the column density. Our targets generally lie at larger distances and thus our sightlines have intrinsically more gas along the line of sight. This difference is also due to the fact that our sightlines contain several clouds, which are unresolved in the *FUSE* data.

Figure 3 also gives some general information about the composition of the LISM. Not surprisingly, the highest column densities are observed in the most abundant metals, O I and N I. These high column densities also indicate that the LB, known mostly for its hot gas that emits soft X-rays, nevertheless still has a substantial amount of neutral gas. Ar I appears to be deficient with respect to O I, suggesting that some of the gas is partially ionized (see § 6). Si II and Fe II have similar solar abundances, but their column density distributions clearly show that Fe II is deficient with respect to Si II, suggesting that Fe is more depleted onto dust grains. P II is much less abundant than Fe II and Si II, but a comparison with the solar abundance (~ -2 dex with respect to Fe II and Si II) implies that Fe and Si are depleted onto dust grains, and hence dust in the form of silicate and iron grains must be present in the LISM (see § 7).

5. MOLECULAR CLOUDS IN THE LISM

5.1. Previous Studies

Copernicus was the first satellite to probe the H₂ Lyman and Werner lines in absorption (Spitzer et al. 1973). Spitzer, Cochran, & Hirshfeld (1974) presented H₂ results toward 28 stars lying between 110 pc and 2 kpc (we corrected these distances with the parallaxes measured by *Hipparcos*). Seven of these stars are situated between 111 and 166 pc and are presented on the Galactic sky in Figure 1 with the symbol “C”. After *Copernicus* was decommissioned, CO emission was the primary technique used to probe molecules in the LISM. Magnani, Blitz, & Mundy (1985) discovered a very large number of CO clouds at high galactic latitude $|b| \geq 20^\circ$, and based on statistical arguments estimated that these clouds (known as MBM clouds) are within 100 pc. Two of these clouds, known as MBM 12 ($(l, b) = (159^\circ, -34^\circ)$) and MBM 16 ($(l, b) = (172^\circ, -38^\circ)$) clouds were considered until recently to be the nearest known molecular clouds to the Sun, at a distance of ~ 65 pc and $60 \lesssim d \lesssim 95$ pc, respectively (Hobbs, Blitz, & Magnani 1986; Hobbs et al. 1988). However, two recent independent estimates of the distance place the cloud MBM 12 at 275–300 pc (Luhman 2001; Andersson et al. 2002), i.e. at a much larger distance than initially thought. These recent results could imply that the MBM clouds might be farther away. Dame et al. (1987) presented a CO survey of the Galaxy at $|b| \lesssim 30^\circ$, but the clouds studied

were estimated to be farther away, $d \gtrsim 140$ pc. Trapero et al. (1996) also found two other molecular cloudlets in ^{12}CO emission in the Galactic plane within 120 pc, $(l, b) \sim (149^\circ, -5^\circ)$.

Direct evidence of H_2 in the LISM has been made possible again with the recent launch of *FUSE*. Note that because H_2 is observed in absorption, the distance to the star directly places a firm upper limit on the distance of any molecular cloud. Recently, Gry et al. (2002) used *FUSE* data to study H_2 in three lines of sight passing through the Chamaeleon complex $((l, b) \sim (300^\circ, -15^\circ))$, which has an estimated distance of 150 pc.

5.2. Distribution of H_2 in the LISM

Although the *FUSE* instrument is sensitive to H_2 columns down to low values, $\sim 10^{14} \text{ cm}^{-2}$, there appears to be detectable amounts of H_2 along six sightlines out of 31 in our sample (Table 5 summarizes the results). The sightlines have distances between $94 \lesssim d \lesssim 159$ pc and lie at $60^\circ \lesssim l \lesssim 120^\circ$ and $-30^\circ \lesssim b \lesssim 40^\circ$ (see Figure 1). We also examined the lower signal-to-noise data from the Z903 program (see § 2.1). The only two stars in the program (at the time of this work) that show H_2 in their spectra are WD 0421+740 $((l, b) = (136.13^\circ, +16.81^\circ), d = 257$ pc) and WD 1725+586 $((l, b) = (87.22^\circ, +33.92^\circ), d = 114 \pm 23)$.⁷ There is, however, no H_2 detection toward 3 other WDs lying in this region of the sky (WD 1820+580, WD 1845+683 [$d = 125$ pc], WD 1943+500 [$d = 98$ pc]). We also note that H_2 was detected toward Feige 110 at even higher latitude $((l, b) = (74.09^\circ, -59.07^\circ), d = 179 \pm \frac{265}{67}$ pc, Friedman et al. 2002). These diffuse H_2 clouds roughly lie in the same direction as that of some of the CO detections. Finally, another star which was not used in our study of atomic and ionic column densities, WD 0441+467 $((l, b) = (158.49^\circ, +0.47^\circ), d = 110$ pc), has very strong H_2 transitions with a larger number of rotational levels compared to the other sightlines. This cloud could be related to the two CO clouds observed by Trapero et al. (1996, see below).

Most or all of the H_2 detected in this study may be close to the boundary of the LB or outside it. Of the six sightlines in Table 5, one, WD 1636+351, has an O I column indicating it is close to the inside of the LB wall, $\log(N(\text{H I})) = 19.2$ dex. The others are 0.3 to 1 dex higher. It is also possible to compare detections and non-detections along neighboring sightlines. Some of the Copernicus sightlines (Spitzer, Cochran, & Hirshfeld 1974) that show H_2 are marked with a ‘‘C’’ in Figure 1. Four of them are close to WD 1615–154 where no H_2 was detected. As shown in Figure 1, WD 1800+685 ($d = 159$ pc), which is listed in Table 5, is near WD 1631+781 ($d = 67$ pc), which shows no detectable H_2 . Likewise, WD 2011+395 ($d = 141$ pc) and WD 2247+583 ($d = 122$ pc), also listed in Table 5, are close to WD 2111+498 ($d = 50$ pc), which shows no H_2 . Although small-scale structure in the medium could cause these differences, it is likely that the molecular clouds reported here reside at distances between ~ 60 pc and ~ 140 pc. Using the Na I D2 contour map

of Sfeir et al. (1999) (their Figure 3), toward the general direction of WD 1615–154 ($l \approx 350^\circ - 0^\circ$) the edge of the LB is about 90 pc, while it is about 65 pc toward the general direction of WD 1631+781 and WD 2111+498 ($l \approx 90^\circ - 110^\circ$). We are forced to conclude on the basis of both the O I column densities and distance considerations, that aside from WD 1636+351, which appears to be just at the wall, there is no evidence in the present data set for molecular clouds within the LB. We note, however, that Sfeir et al. (1999) found dense, cold clouds toward this direction at ~ 85 pc.

5.3. Properties of the Observed H_2

The total H_2 column densities are modest ranging from $1.7 \times 10^{14} \text{ cm}^{-2}$ toward WD 2011+395 to $2.4 \times 10^{15} \text{ cm}^{-2}$ toward WD 2148+286. Toward the other sightlines in our sample, the H_2 amount is less than $\sim 10^{14} \text{ cm}^{-2}$. These column densities are generally smaller than the ones derived by Spitzer, Cochran, & Hirshfeld (1974) (2 sightlines have $\log N(\text{H}_2)$ between 14.5 and 15.3 dex, the others marked in Figure 1 have $\log N(\text{H}_2) \gtrsim 19$ dex).

The molecular fraction is defined as $f_{\text{H}_2} \equiv 2N(\text{H}_2)/[N(\text{H I}) + 2N(\text{H}_2)]$. To obtain the values for the H I columns, we use O I as a proxy, except toward WD 2148+286 which has a good H I determination (Sonneborn et al. 2002). The molecular fractions obtained range between 5.0×10^{-6} and 1.4×10^{-4} and are comparable to values obtained for other Galactic sightlines with $\log[N(\text{H I}) + 2N(\text{H}_2)] \lesssim 20$ dex (Savage et al. 1977). We note that these sightlines do not have higher depletion onto dust grains compared to the other sightlines (see § 7).

In contrast, Trapero et al. (1996) found $N(\text{H}_2) \sim N(\text{H I}) \sim \text{few} \times 10^{20} \text{ cm}^{-2}$ toward Perseus $((l, b) \sim (149^\circ, -5^\circ), d \sim 120$ pc) from ^{12}CO measurements. The *FUSE* data for WD 0441+467, discussed in § 5.2, indicates a large amount of H_2 probably at a level of a few times 10^{19} – 10^{20} cm^{-2} .⁸ The stars observed by *Copernicus* are also at similar distances and also have H_2 column densities between 10^{19} – 10^{20} cm^{-2} (Spitzer, Cochran, & Hirshfeld 1974). This indicates that the LISM has a higher density in this direction at relatively close distances.

We find that all the rotational levels can generally be fit with a single excitation temperature, $T_{\text{ex}} \approx 300$ K (see Table 5), a value that represents all of the sightlines well. This follows the results of Spitzer, Cochran, & Hirshfeld (1974) where they found if $N(J=0) \lesssim 10^{15} \text{ cm}^{-2}$, a single excitation temperature generally fits all the observed $N(J)$. The value of T_{ex} reported in Table 5 compares favorably with the results of Spitzer, Cochran, & Hirshfeld (1974). Note that they also found one sightline (τ Sco) with a similar total H_2 column density (14.56 dex) but with a much larger $T_{\text{ex}} \sim 1013$ K.

The H_2 b -values for the 6 sightlines in our sample range from 2.8 to 5 km s^{-1} . This is smaller than the b -values derived for O I and N I which are generally larger than 5 km s^{-1} (see Table 3). The parameter b is usually defined as $b = \sqrt{2kT/(Am) + v_{\text{turb}}^2}$, where the symbols have their usual meaning. So if H_2 and O I (or N I) were in the same

⁷ The distance for WD 1725+586 is from J. Dupuis (2002, private communication). For the other sightlines mentioned in this section the distances are from Holberg, Barstow, & Sion (1998) or Vennes et al. (1998) unless otherwise mentioned.

⁸ This star was not considered for this survey because the large contamination of molecular lines and stellar lines, but clearly a detailed analysis of this sightline would be very interesting.

gas phase, one would expect to have $b(\text{O I}) < b(\text{H}_2)$, since the mass of H_2 is lower than that of O. This is not the case, and it would seem to imply that H_2 is in a different phase. However, some of the higher values for $b(\text{O I})$ might be explained by the presence of several components separated in velocity but not all detected in H_2 . The H_2 b -values indicate a thermal temperature less than 900–3000 K, different from the temperature of 7000 K observed usually in the local interstellar gas. The O I column densities and distances of these sightlines place these clouds near the wall of the LB or beyond. This would appear to be in agreement with H_2 tracing colder neutral gas and hence with smaller b -values.

All the sightlines showing H_2 in our survey are located in roughly the same area, with similar upper limit distances or, as discussed in § 5.2, ranges of distances. They also have similar column densities, molecular fractions, excitation temperatures, and b -values. These facts suggest that the gas studied could be the same large diffuse cloud, possibly in form of an extended thin sheet.

Combining these results imply that the H_2 clouds in the LISM can be in form of diffuse clouds, but there are regions (not explored with our survey) where there is enough gas and dust to shield the interstellar radiation field, allowing a large molecular fraction to form (see, Trapero et al. 1996).

6. IONIZATION OF THE LISM

6.1. *The Neutral Species*

6.1.1. *Background*

Recent studies of the neutral species in the LISM reveal that they could constrain the origin (photoionization or non-equilibrium cooling) of the ionization (Sofia & Jenkins 1998; Jenkins et al. 2000). The argument of Sofia & Jenkins (1998) is that a deficiency of Ar I is not caused by Ar depleting into dust grains, but rather its neutral form can be more easily photoionized than H. The photoionization cross-section of Ar is about 10 times that of H over a broad range of energies, so Ar can be more fully ionized than H in a partially ionized gas. While in dense regions N behaves like O, i.e. the ionization fractions of these elements are strongly coupled with the ionization fraction of H via a resonant charge-exchange reaction, in low density, partially ionized regions N behaves more like Ar by showing a deficiency of its neutral form. N also is not depleted onto dust grains (Meyer, Cardelli, & Sofia 1997). On the one hand, if a region was highly ionized at some earlier epoch, by say a shock, and is in the process of recombining, then Ar I, (N I) and H I would have about the same ionized fraction because the recombination coefficients are roughly the same. On the other hand, if steady photoionization dominates, then Ar I should be deficient from the arguments mentioned above. If the region is low density and ionized, N I will also be deficient.

We first describe the results that the data show in this section and § 6.2. We will discuss more thoroughly their meaning and their implications with new ionization calculations in § 6.3.

Figure 4 presents the ratios of Ar I/O I, N I/O I, and (N II+N I)/O I plotted versus the total column density of O I and the distance of the sightline. Both Ar I and N I show deficiencies with respect to O I toward many of

the sightlines but the scatter is large. We also plot in this figure the B-type star and solar abundances for Ar/O, and B-type star, solar, and interstellar abundances for N/O.

The reference abundances of Ar are from Keenan et al. (1990) and Holmgren et al. (1990) for B-type stars, and from Anders & Grevesse (1989) and Meyer (1989) for the solar abundance. The solar O and N abundances are from Allende Prieto, Lambert, & Asplund (2001) and Holweger (2001), respectively. We note that Holweger (2001) also derived an O solar abundance, but with a higher uncertainty than Allende Prieto, Lambert, & Asplund (2001). In any case the difference between these two values is 0.05 dex and does not change any of our conclusions. The interstellar O and N abundances are from Meyer, Jura, & Cardelli (1998) and Meyer, Cardelli, & Sofia (1997), respectively (the interstellar abundances were typically measured for more distant sightlines with higher hydrogen column densities, $20.2 \leq \log N(\text{H I}) \leq 21.2$). For the O and N abundances in B-type stars see Sofia & Meyer (2001) and references therein. Table 6 summarizes the Ar I/O I and N I/O I ratios measured in this study, normalized to the solar abundances for reference.

6.1.2. *Nitrogen and Oxygen*

The N I/O I ratio versus the distance presented in Figure 4 does not show any particular trend, probably primarily because the interstellar clouds are not resolved and the exact distance of the clouds remains unknown. However, when considering the sightlines for which the clouds are well within the LB ($\log N(\text{O I}) \lesssim 15.60$), N I/O I is systematically down to -1.00 ± 0.07 dex (compared to the interstellar ratio in denser clouds of -0.66 dex and to the solar value of -0.76 dex). Once $\log N(\text{O I}) > 15.60$ dex, i.e. the gas is near or beyond the edge of the LB, the picture is far more complicated, with a scatter of N I/O I between -1.1 dex and the interstellar value obtained for sightlines with much higher column densities; N I/O I varies over 0.45 dex in the LISM.

The bottom panel of Figure 4 shows clearly that measurements or lower limits of (N II+N I)/O I are much closer to a normal interstellar N/O ratio. The deficiency of N is therefore explained by ionization of this element. In the LB, the amount of N II can be as large as ~ 3 times the amount of N I. Several limits or values of (N II+N I)/O I are above the interstellar N/O ratio, suggesting that O can be partially ionized in significant quantities as well.

The last column in Table 6 gives the ratio of N I/(N I+N II). There is a measured value of this ratio toward 5 stars. For the four of them which are well inside the LB ($\log N(\text{O I}) \lesssim 15.60$) the measured ratio implies that from 40% to 70% of N is ionized, while in the sightline located near the edge of the LB ($\log N(\text{O I}) = 15.78$) only 5% of the N is ionized. The upper limits show, depending on the direction, that at least 2% to 75% of N can be ionized. Combining the upper limits and the measurements suggests that the ionization conditions are not uniform in the LB (even though N I/O I appears fairly constant).

6.1.3. *Argon and Oxygen*

For most sightlines, the Ar I/O I ratio also shows a deficiency of Ar I in the LB by ~ -0.3 dex with respect to the solar value when $\log N(\text{O I}) < 15.60$ dex, but with

a larger scatter than the scatter observed in N I/O I. Ar I/O I is near solar for the WD 1634–573 sightline with $\log N(\text{O I}) = 15.51$ dex. Wood et al. (2002a) using GHRS G230M observations suggest that there could be at least two clouds along WD 1634–573. The amount of N II is actually larger than the amount of N I by a factor 2 toward WD 1634–573, even though the N I/O I is the highest in the LB sample. It seems therefore plausible that one of these clouds is largely ionized, while the other one is mostly neutral. This explains why N I/O I and Ar I/O I are near solar, since these atoms exist predominantly in the neutral cloud. In addition, the super-solar and super-interstellar ratios for (N II+N I)/O I and the low N I/(N II+N I) ratio indicate a deficiency of the neutral form of O and N, and thus the presence of a substantially ionized cloud along this line of sight (this is also confirmed by the strong C III line, see § 6.2). Hence, a near solar ratio for Ar I/O I does not necessarily imply that there is no ionized cloud along the sightline.

Near the edge of the LB and beyond, the scatter of the Ar I/O I becomes larger, ranging from a solar value to -0.8 dex subsolar. In the Local Cloud within ~ 5 pc from the Sun, Ar II is the dominant ion according to the photoionization calculation by Slavin & Frisch (2002). The scatter in the Ar I/O I ratios is large, either plotted with respect to the O I column density or the distance and is larger than the scatter of N I/O I.

The Ar II line can be found at 919.781 \AA , which is within the FUSE spectral range. However, the data in this wavelength region are usually of lower quality and this line is too weak to be detectable in the spectra studied here. Sofia & Jenkins (1998) show that Ar was very unlikely to be depleted onto dust grains. Therefore we conclude that the observed deficiency of Ar I found for almost every sightline in our study of the LISM is due to photoionization.

6.1.4. Nitrogen and Argon

In Figure 5, we compare the ratios of [Ar I/O I] and [N I/O I] normalized to their solar values⁹ but only for data with 1σ error $\lesssim \pm 0.30$ dex, i.e. only with the higher quality measurements. This plot confirms that N I and Ar I are deficient compared to their respective solar values. With only a few exceptions, $[\text{N I/O I}] \gtrsim [\text{Ar I/O I}]$. This result can be explained by the fact that Ar is more easily ionized than N because of its larger ionization cross section. There are, however, several data points that suggest that N I could be as efficiently ionized as Ar I. Figure 3 of Sofia & Jenkins (1998) suggests that for ionizing photons energies $E > 35$ eV, N could be more easily ionized than Ar. But with the constraint from C III/C II measured in this study and with new ionization calculations, it appears difficult to satisfy this condition in the LISM. We will return to a discussion of [Ar I/O I] and [N I/O I] in the context of a photoionization model in § 6.3.

6.2. The Ionized Species

The singly ionized species measured in this work are in the dominant ionization stage in both the neutral and ionized gas, and therefore cannot tell us directly much about the ionization conditions in the LISM. There are, however,

⁹ Hereafter, $[X/Y]$ refers to an abundance ratio in logarithmic solar units, $[X/Y] = \log(X/Y) - \log(X/Y)_{\odot}$.

detections of C III along nearly every sightline and one detection of Fe III toward WD 1800+685. The production of C III by photoionization requires photons with energies greater than the C II ionization threshold of 24.4 eV. At energies above 47.9 eV, C III is ionized to C IV. For the production of Fe III, the Fe II threshold is 16.2 eV and the Fe III threshold is 30.7 eV. As discussed in § 6.3, C III, in particular, is a good tracer of ionized gas.

Unfortunately, usually both the C II and C III lines are saturated, and only a few meaningful limits and measurements are presented in Table 7. In this Table, we also list the values or range of values of C III after correction for blending of the interstellar line with the stellar C III line. We modeled the synthetic spectra by using either the C III excited lines at 1175 \AA or using C IV available with IUE. In some cases, we were only able to estimate a limit and hence only a range of possible values.

Toward WD 1634–573 the value of C III/C II is relatively high, about -0.63 dex, confirming the presence of a largely ionized cloud along this sightline, possibly a H II region around the star. For all the other sightlines the ratio is less than or of the order of -1 dex; and toward WD 1314+293 this ratio is very weak, -2.24 dex. The sightlines for which we were able to measure C III/C II lie well within the LB. However, Tables 4 and 7 show that C III appears to be ubiquitous in the LISM toward our sightlines. We note, however, that toward several more nearby stars, C III was not detected (Redfield et al. 2002), implying that either the ionization conditions change in more distant sightlines or that C III might arise partly from H II regions near the WDs. While C III/C II appears to vary from sightline to sightline, unlike what we found for N II/N I, the fraction of C III with respect to C II is generally small. The recent ionization calculations of Slavin & Frisch (2002) of the Local Cloud within 5 pc of the sun show that C III/C II ~ -1.44 dex (model 17, their Table 8), in general agreement with our measurements. Our observations typically probe denser clouds. Possibly a significant fraction of the clouds are neutral regions, where C II is also dominant. These observations demonstrate that C III, while present, is not a dominant ion in the LISM.

While we generally have a good measurement of Fe II, Fe III is either undetected or can be blended with photospheric lines. Only one measurement, $\log[N(\text{Fe III}/N(\text{Fe II}))] \sim -1.2$ dex, was obtained toward WD 1800+685 which probably lies beyond the wall of the LB. This result and the other limits are summarized in Table 8. Slavin & Frisch (2002) found with their ionization calculations Fe III/Fe II ~ -1.40 dex (model 17, their Table 8), which, as for C III, shows an agreement with our measurements and indicates that Fe II is the dominant ion in the LISM.

6.3. Ionization Calculations and Implications

To obtain more quantitative insights, we developed the photoionization code used by Sofia & Jenkins (1998) and Jenkins et al. (2000). The detailed equations and how they are solved are fully described in Sofia & Jenkins (1998). But here, in all cases, the formulae included the effects of

units, X and Y represent the column densities of two elements:

charge exchange with neutral hydrogen and the modifications of the H and He ionization fractions. We modified several parameters in the program that created Figure 2 in Jenkins et al. (2000) in the following ways:

(1) We replaced the hot gas interface radiation given by Slavin (1989) with the spectrum calculated by Slavin & Frisch (1998). This new spectrum shows more details at high photon energies, and the physical conditions for the Local Cloud seem more realistic. The new spectrum is about 5 times more intense than the old one. This slightly increases the ionization inside the cloud. We are assuming that more distant clouds have properties similar to those that we know exist for the Local Cloud. Likewise, we assume that the radiation field due to the WDs is the same everywhere and is that reported for the local neighborhood by Vallerga (1998) using *EUVE* observations.

(2) The upper limit for the H I absorbing column densities has been increased to somewhat above 10^{19} cm^{-2} , on the assumption that some lines of sight could be dominated by monolithic clouds with this column density. This upper limit approximately corresponds to the median column density of O I that we found in this survey. In all likelihood, the higher column density cases are composed of several clouds that have less shielding than a few times 10^{19} cm^{-2} of neutral hydrogen. In addition, the complex non-spherical geometry of a cloud may reduce the effective shielding to absorbing column densities much lower than the value implied by the measurement along the sightline.

(3) We added the atomic parameters for C, P, Si, S, and Fe. In particular, we plot explicitly the values of C III/C II and Fe III/Fe II.

The results are plotted in Figure 6 as a function of the absorbing column shielding in the external ionizing radiation sources. A uniform pressure within a given cloud of $p/k = 2.5 \times 10^3 \text{ cm}^{-3} \text{ K}$ is assumed. This pressure is consistent with the pressure derived by Gry & Jenkins (2001) toward ϵ CMa. Reducing the pressure would give a C III/C II ratio that is too high with respect to the observed values.

Figure 6 illustrates how O I follows H I very well, while N I and Ar I become progressively more deficient as the shielding from hydrogen decreases. The other elements (C, P, Si, S, and Fe) remain primarily in the singly ionized state, but the abundances of these ions are elevated relative to that of neutral hydrogen. The assumed pressure seems to give a reasonable set of values for C III/C II, but Fe III/Fe II appears to be too low. Yet, we have only one measurement and this measurement is very uncertain (see § 6.2). In contrast, Slavin & Frisch (2002) found similar fractions for C III/C II and Fe III/Fe II in their model. Except for this discrepancy, these two models are in reasonable agreement. According to our model, the fraction of Fe III is heavily dependent on the effect of charge exchange with neutral hydrogen. This is not the case for C III. Without taking into account the effect of charge exchange with neutral hydrogen, the fraction of Fe III is comparable to the fraction of C III. Therefore, the amount of Fe III depends on the density and ionizing radiation field, making Fe III a less reliable tracer of ionized gas compared to C III.

In Figure 5, the model predictions are compared with the measured ratios of [N I/O I] and [Ar I/O I]. There is

a large scatter in the measurements due to the scatter in the physical properties of the different clouds. The model assumes the same physical properties for all clouds. The study reported here and many others (e.g., Gry & Jenkins 2001; Redfield et al. 2002) demonstrate that this is not the case. Nevertheless, it should be noted that, within 1σ error, the majority of the data points agree with our model.

For about 6/22 data points in Figure 5, [Ar I/O I] is significantly higher than predicted and thus is approximately equal to [N I/O I]. This suggests that, for these sightlines, the ionization fraction of N could be as large as that of Ar. Using our model, we have explored several combinations of parameters by varying the pressure and ionizing flux to see if we could reproduce such ionization fractions. First, the value of p/k must be well below $10^3 \text{ cm}^{-3} \text{ K}$ to make the electron density high enough (and $n(\text{H I})$ low enough) in order to have the charge exchange relatively inefficient between nitrogen and hydrogen. Moreover, the spectrum of the ionizing radiation must be altered drastically, e.g., with a very strong flux of photons (of unknown origin) that have an energy $E \gtrsim 35 \text{ eV}$ (see Figure 3 of Sofia & Jenkins 1998). Perhaps these photons originate from the recombination of He II. When all of these extreme conditions are invoked, the ionization of N can even be slightly higher than that of Ar. However, under those conditions C III/C II becomes far too large compared to our result. So with our model, a higher or comparable ionization fraction of N compared to that of Ar is difficult to explain with a simple photoionization phenomena. Assuming collisional ionization equilibrium in a hot plasma, Shull & van Steenberg (1982) calculated the expected deficiency of the neutral forms of Ar, N, and O. According to their values, collisional ionization of these elements would not appear to solve this problem. While in principle O can be depleted by about 25% (Moos et al. 2002), Ar and N are very unlikely to be depleted by any significant amount (Sofia & Jenkins 1998; Meyer, Cardelli, & Sofia 1997). Another possibility would be an overabundance of Ar in certain directions. But that would seem to be difficult to reconcile with no apparent changes in abundances for the other elements, especially the α -elements such as O.

While our model might be too naive to reproduce the different changes in the physical conditions occurring in the LISM, our observations strongly indicate that photoionization is a major ionization contribution in the LISM. These results do not support the proposition that the LISM is in the process of recombining from an highly ionized phase at some earlier epoch, in which case Ar I and N I and H I would be roughly equally ionized. The photoionization conditions may not be constant in the LB and more generally in the LISM according to the variation observed in Ar I/O I, N I/O I, N I/(N I+N II), and C III/C II. But this is complicated by the unresolved cloud structure. For example, toward WD 1634–573, at least two clouds are present with one of them being substantially ionized (large C III and N II fractions; possibly an H II region near the star) and the other one mostly neutral (near solar abundance for Ar I/O I and N I/O I). Another example is toward WD 1314+293, where there is a large fraction of N II but a very small fraction of C III.

7. DUST IN THE LISM

Several studies have examined the deficiency of elements in the gas-phase of the Galaxy with respect to solar or B-type star abundances (see the review by Savage & Sembach 1996a, and references therein). When ionization is not the cause, these deficiencies are called depletions and are usually explained by the fact that certain elements are preferentially locked up into dust grains. These studies show a general progression of increasingly severe depletion from warm halo clouds, to warm disk clouds, to colder disk clouds. Below, we will compare these observed depletion patterns with studies of other parts of the Galaxy. S II (or Zn II) or H I are often used because the former two are lightly or not depleted onto dust grains and the latter gives the absolute gas-phase abundance directly (when ionization is not important). S II and Zn II are not available in the FUSE wavelength range, and as discussed in the § 6, the LB and LISM are partially ionized, therefore using O I as a proxy for H is not suitable. However, we show in § 6.3 that as long as conditions are not extreme, the other elements (C, Si, P, and Fe) appear to remain primarily in the singly ionized state. This is also confirmed by the photoionization calculations of Slavin & Frisch (2002). Therefore the abundance of C II, Si II, P II, and Fe II can be compared directly in order to measure the depletion onto grains. We note that this method of sensing the existence of dust relies on the underlying assumption that the reference abundances of the elements apply to the LISM. Direct detection of dust grains within the solar system were made possible using the *Ulysses* and *Galileo* satellites and are discussed by Frisch et al. (1999).

Previous studies show that P is only lightly depleted onto dust grains especially in warm gas (e.g., Welty et al. 1999). However, P II is 2 or 3 orders of magnitude less abundant than the other species, so that only a few measurements were possible in our survey. On the other hand, C is very abundant and is lightly depleted. Because of this and the fact that C is so abundant and the only available transition of C II is so strong, a measurement of the column density of C II was possible toward only a few sightlines with low columns (the high velocity components have all low column densities and are discussed in § 9). Si II and Fe II are both depleted into dust grains, and they are easily measured in our survey.

Evidence for dust grains in the LB and beyond is shown in Figure 7 where the logarithmic ratios of $N(\text{Fe II})/N(\text{Si II})$ and $N(\text{P II})/N(\text{Si II})$ are shown. Even though P is the least depleted amongst these three elements and would then be a better element for reference, we chose Si because there are many more measurements in common with Fe. The solar (meteoric) values of these ratios are -0.04 and -1.98 dex for Fe/Si and P/Si, respectively (Anders & Grevesse 1989). Except for one value that could be compatible with a solar value within the error bars (WD 2011+395), [Fe II/Si II] is depleted from about -0.3 to -0.8 dex, typical of what is observed in “cold-warm” and “halo” clouds (Savage & Sembach 1996a, and references therein). Note that for Fe/Si it is not possible to differentiate between a cold and a warm depletion pattern, since it is depleted in both types of gas by ~ -1 dex. Figure 7 shows that there is no difference between the interstellar clouds within the LB, near the wall, or beyond.

In particular the range of values over which [Fe II/Si II] varies is similar.

[P II/Si II] varies generally from a solar value (-2.0 dex) to -0.8 dex. This is also similar to depletions observed either in “cold” or “warm-halo” clouds (Savage & Sembach 1996a). Note that in this case the warm and halo depletion patterns can not be differentiated from each other (there is only an estimate of the depletion of P in halo gas). Only two values are available within the LB: a solar value and -0.3 dex below solar.

Plotting the results for [P II/Si II] and [Fe II/Si II] for common sightlines could *a priori* differentiate between the different depletion patterns since the cold, warm, and halo depletion patterns have different locii. Figure 8 shows [P II/Si II] versus [Fe II/Si II] along with the expected depletion patterns observed in more distant sightlines in the Galaxy. Most of the clouds appear to be dominated by more warm-like or halo-like gas than cold gas. The scatter is probably mainly explained by the fact that the clouds are not resolved and therefore are a combination of different gas phases. The sightline toward WD 0131–163 is more complicated to understand because [P II/Si II] points toward a cold depletion pattern while [Fe II/Si II] toward an halo depletion pattern.

The solar ratios of Si/C, P/C, Fe/C are -1.00 , -2.98 , -1.04 , respectively. Toward the few sightlines where a measurement of C II was possible, the ratios ([Si II/C II], [P II/C II], [Fe II/C II]) are: $(0.18, < 1.40, < -0.13)$ toward WD 0549+158, $(< 0.05, < 1.64, < -0.06)$ toward WD 1254+224, $(-0.98, < 0.12, -1.62)$ toward WD 1314+293, $(-1.14, -0.84, -1.78)$ toward WD 1634–573. The two first sightlines do not have any stringent limits. Toward WD 1314+293, these ratios are compatible with a cloud having a cold depletion pattern (in agreement with the ratios of P/Si and Fe/Si). These ratios for WD 1634–573 point also to a cold depletion pattern ([P II/C II] is, however, far too small), but this is in contradiction with the results from P/Si and Fe/Si (see Figure 8), which might suggest that there is a lack of dust containing C toward this sightline.

The main reason for the deficiencies of Si and Fe are understood to be due to the incorporation of some of the Fe and Si into dust grains. The scatter in the values may reflect changes in the dust fraction or complications in the ionization fractions that are similar to those that we found for N, Ar, and O. The fact that we do not observe any trend with the distance or total column density of the sightline is probably mainly due to the fact that the clouds are not resolved.

8. ELECTRON DENSITY AND COOLING RATE IN THE LISM

8.1. Electron Density

If collisions with electrons are the principal source of fine-structure excitation of C II in the LISM, then the familiar collisional equilibrium equation between C II and C II* (e.g., Gry & Jenkins 2001) can be simplified to

$$n_e = 0.189 T^{0.5} \frac{N(\text{C}^{+*})}{N(\text{C}^+)} \text{ cm}^{-3}, \quad (1)$$

when $N(\text{C}^{+*}) \ll N(\text{C}^+)$ and $T \gg 93$ K. This relation provides an estimate of the electron density when the space densities are replaced by column densities. The collisions

with neutral hydrogen atoms should not be significant in the LISM. Indeed, according to Fig. 3 of Keenan et al. (1986), $n(\text{H I}) = 1.0 \text{ cm}^{-3}$ alters the inferred electron density only when $\log[N(\text{C}^{+*})/N(\text{C}^+)] \lesssim -2.7$, but our calculations indicate that $n(\text{H I}) < 0.3 \text{ cm}^{-3}$ in the LISM as long as $p/k \leq 2500 \text{ cm}^{-3} \text{ K}$ (see Figure 6).

There is no evidence of C being depleted into dust in the LISM (see § 7). P is also known to be only lightly depleted. Moreover, in other regions of the Galaxy, C and P have similar depletions (Savage & Sembach 1996a). Differences in ionization of C and P are probably not important ($N(\text{C III})$ is small with respect to $N(\text{C II})$; see § 6 and Figure 6), so that we can write $\log[N(\text{C II}^*)/N(\text{C II})] \approx \log N(\text{C II}^*) - \log N(\text{C II}) + \log(\text{P/C})_{\odot}$, where the solar ratio $\log(\text{P/C})_{\odot} = -3.0$ dex.

Under these assumptions and assuming a temperature of $T = 7000 \text{ K}$ observed in LIC, we can determine the electron density. This is shown in the bottom panel of Figure 9. The mean value is $n_e \lesssim 0.1 \text{ cm}^{-3}$. Toward Capella situated at a distance of $d = 12.9 \text{ pc}$, Wood & Linsky (1997) determined $n_e = 0.05\text{--}0.23 \text{ cm}^{-3}$. We also plot in Figure 9 the expected electron density from our model versus the shielding of H I (see § 6). All the points fall above this line, suggesting that they are probably multiple regions where the shielding in each region is much less than the total column density of the sightline.

8.2. Cooling Rate

Because carbon has a high abundance, one of the most efficient way for cooling the diffuse gas is via the excitation of the C II by collisions with electrons and hydrogen atoms followed by the spontaneous emission at $157.7 \mu\text{m}$ when the levels decay to the ground state. It follows that the C II cooling rate in ergs^{-1} per H I atom can be written (e.g., Savage & Sembach 1996b),

$$l_c = 2.89 \times 10^{-20} \frac{N(\text{C}^{+*})}{N(\text{H}^0)}, \quad (2)$$

where $\log N(\text{H I}) = \log N(\text{O I}) + 3.5$ (see § 4). In those conditions, the mean value in our sample is $\log l_c = -25.59 \pm 0.32$ dex. Using P II as a proxy for the total H (H I+H II) and assuming no depletion, we have $\log l_c = -25.30 \pm 0.39$ dex in our sample. If a depletion of ~ -0.2 to -0.3 dex is assumed for P (Savage & Sembach 1996a; Welty et al. 1999), both determinations are in good agreement. This result is in agreement with previous determinations derived in the diffuse gas in other parts of the Galaxy via different methods (Gry, Lequeux, & Boulanger 1992; Bock et al. 1993; Savage & Sembach 1996b; Boulanger et al. 1996). Toward Capella, using the H I and C II* column densities from Wood et al. (2002b), $\log l_c = -25.14 \pm 0.03$ dex, but increases by about 0.3 dex when using O I as a proxy of H I.

In the top panel of Figure 9, we show the cooling rate against the total H I column density, showing a clear anticorrelation between these two quantities. This likely indicates that for low column density sightlines, a substantial amount of C II is associated with ionized gas, which is not taken into account in the normalization by the $N(\text{H})$ column density.

9. HIGH VELOCITY COMPONENTS

The sightlines toward WD 0455–282, WD 1202+608, and WD 1528+487 each show a high velocity component separated by -56 , -40 , and -39 km s^{-1} , respectively, with respect to the lower velocity component. In the different tables, the high velocity component is designated by the letter “a” after the star name. Toward WD 0455–282 and WD 1528+487, high velocity components are clearly detected only in the C II absorption line for the elements considered here. For WD 0455–282, there is also a clear detection of this component in the H I Lyman lines. For WD 1528+487, there is only a hint in the Lyman lines. This rules out misidentification due to a stellar line. For these two stars, the presence of C II absorption features and the non-detection of neutral species, in particular the strong O I $\lambda 1039$ line, implies that these clouds are mostly ionized.

Toward WD 1202+608, several species are detected (see Table 4), making the identification as a high-velocity component unquestionable. In contrast to the two other sightlines which have a very low column density with respect to their low velocity counterparts, this cloud has comparable column densities compared to the lower velocity components for Si II and Fe II. However, it has much smaller column densities for the neutral species, O I and N I, implying that this cloud is predominantly ionized. In addition, $N \text{ I}/(N \text{ II}+N \text{ I}) < 0.09$, showing that at least 91% of N is in an ionized form. A similar comment applies for Ar I, even though the result remains more uncertain for this atom. Unfortunately, we have no information for C III and Fe III, because the former is blended with the local component (but the large lower limit – the largest in our sample – suggests a fair amount of C III), and Fe III is confused by the moving stellar lines from this binary system. The column density of O I suggests an H I column density of ~ 18.20 dex, while Si II gives a total H column density of > 18.6 dex (it is a lower limit because Si can be substantially depleted onto dust grains), implying an H II column density > 18.3 dex.

Holberg et al. (1995) and Kruk, Chayer, & Dupuis (2003) argue that the origin of the high velocity component toward WD 1202+608 may be a remnant from the ejected common envelope of the binary, assuming it is a relatively young system. Gry & Jenkins (2001) also identified two negative high velocity components in the line of sight toward $\epsilon \text{ CMa}$ at -27 km s^{-1} and -82 km s^{-1} from the main component. The fact that the velocity of these components is always negative would also point toward a circumstellar origin. However, it should be noted that the high velocity features appear in pairs of stars. WD 0455–282 is in the same part of the sky as $\epsilon \text{ CMa}$, and WD 1202+608 is in the same part of the sky as WD 1528+487. This suggests that in each of these two cases, the sightlines could be passing through a single gas cloud. If so, the clouds are probably much closer than the stars and because of the high ionization are likely well within the LB. Although the argument is not definitive, it does weigh against the hypothesis of stellar ejecta. Finally, we note that this study does not show widespread high-velocity components along many sight lines. In particular, there is no evidence of globally expanding gas at positive velocities as might be expected for the case of a recent supernova explosion positioned near the Sun.

10. SUMMARY AND CONCLUDING REMARKS

We present a comprehensive survey of the LISM which includes the main species available in the far-uv wavelength range (C II, C II*, C III, N I, N II, O I, Ar I, Si II, P II, Fe II, Fe III, and H₂). The spectral resolution ($R \sim 20,000$) is not sufficient for detailed analysis of velocity structures. However, the number of species available permit a study of some of the fundamental characteristics of the local interstellar gas by comparing the relative column densities, the ionization structure, the molecular content, and the indirect indication of dust.

Our survey detected only very diffuse molecular clouds ($f_{\text{H}_2} \lesssim 10^{-4}$). H₂ was detected in only six out of 31 sightlines all within a single sector of the sky (see Figure 1). Thus it appears that H₂ is not widely distributed in the LISM. The derived H₂ b -values for the 6 sightlines in our sample range from 2.8 to 5 km s⁻¹, implying thermal temperatures less than 900–3000 K. This is different from the temperature of 7000 K usually observed in local interstellar clouds, implying different gas phases in the LISM. Combining our results with previous work on H₂ in the LISM shows that the molecular phases are not uniform. Molecular hydrogen can exist in diffuse clouds, but in some regions the molecular fractions are similar to the atomic content.

The comparison of column densities of Si II, P II, Fe II provides information on the dust depletions of LISM. The relative abundances of these species vary from sightline to sightline, again suggesting different gas-phases in the LISM. These abundance ratios are better represented by typical warm or halo diffuse clouds observed in more distant sightlines in the Galaxy rather than a cold depletion pattern.

The cooling rate in the LISM, l_c (in erg s⁻¹ H I atom⁻¹, where the H I column density was determined from the O I column density), can be derived directly from the C II* absorption lines and has a mean value of $\log l_c = -25.59 \pm 0.32$ dex, very similar to previous determinations. Higher values are observed at lower H I column densities, indicating that for low column density sightlines, a substantial amount of the C II must come from ionized gas. The electron density can also be inferred from the C II* absorption lines. Using P II as a proxy of C II and assuming a temperature of 7000 K, the electron density in the LISM is $n_e \lesssim 0.1$ cm⁻³, but larger than the values predicted by our model. This disagreement likely indicates that there are multiple regions along the sightlines where the H I shielding in each region is much less than the total H I column density of the sightline.

The comparison of column densities of N I and Ar I to O I provides information on the ionization structure of the LISM. The N I/O I ratio is systematically -0.24 dex subsolar in the LB. Near or beyond the LB boundary, the picture is far more complicated, with a scatter of N I/O I between ~ -0.3 dex subsolar to $\sim +0.15$ dex supersolar (WD 1636+351). Using measured values and lower limits on the N II column densities, we show that the observed deficiencies are likely due to ionization and not abundance variations or dust depletions. For most sightlines, the Ar I/O I ratios also show deficiencies of Ar I in the LB by ~ -0.35 dex with respect to the solar value, but with a larger scatter than for N I, and this scatter increases beyond the LB ranging from a solar value to

~ -0.8 dex subsolar.

More highly ionized species such as C III and Fe III are also available to constrain the ionization structure. C III appears to be ubiquitous in the LISM for our sample, and C III/C II appears to vary from sightline to sightline. The C III/C II ratio is however generally small; C III is not a dominant ion in the LISM. Fe III remains more elusive and is often completely lost in the stellar profile. But our limits on Fe III/Fe II indicate that Fe II is the dominant ion in the LISM.

We modified the photoionization code used by Sofia & Jenkins (1998) and Jenkins et al. (2000). In particular, we adopted the new radiation field calculated by Slavin & Frisch (1998) and added the atomic parameters for C, P, Si, S, and Fe. The calculations were performed for a sequence of models where the thermal pressure was set to a value of $p/k = 2.5 \times 10^3$ cm⁻³ K. These calculations show that O I follows H I very well, while N I and Ar I become progressively more deficient as the shielding from H I becomes smaller. The other elements (C, P, Si, S, and Fe) remain primarily in the singly ionized state. The assumed pressure also seems to give a reasonable set of values for C III/C II. However, the values calculated for Fe III/Fe II appear to be too low, although we have only one measured value of Fe III/Fe II, the rest are upper limits. According to our model, the fraction of Fe III is heavily dependent on the effect of charge exchange with neutral hydrogen and is therefore not a reliable tracer of ionized gas.

Ar I, N I and H I have similar recombination coefficients, so if the LISM was highly ionized at an earlier epoch by a strong shock and is in the process of recombining, these elements would have roughly equal ionized fractions. Our study contradicts this proposition by indicating that photoionization is a major contribution. We note, however, that in a few cases, [N I/O I] is approximately equal to [Ar I/O I], suggesting that the ionization fraction of N could be as large as that of Ar, which contradicts our model. This could indicate the radiation field might be harder in some directions. However, our model does not provide a clear explanation for this phenomenon with respect to the different observational constraints, and other factors are needed to explain this condition (e.g., non-equilibrium collisional ionization or overabundance of Ar possibly due to a supernova).

The variations observed in the ratios of Ar I/O I, N I/O I, N I/(N I+N II), and C III/C II indicate that the photoionization conditions are probably not uniform in the LB and in the LISM. Such changes in the photoionization conditions might be linked to the patchiness observed in the distribution O VI absorption (Oegerle et al. 2003). These variations, in turn, may depend on the strength and direction of the magnetic field at the cloud boundaries. Slavin & Frisch (2002) argued that evaporative interfaces at the boundaries of the clouds (O VI absorption being a tracer of such interfaces) could account for a large fraction of the observed ionization. Better observational constraints will come from higher spectral resolution of far-UV spectra, in which the individual clouds can be resolved.

Finally, we note that our results do not strongly contradict the X-ray data. Juda et al. (1991) compared the Be and B band fluxes in a number of different directions

and found that the ratio of the two did not change with the overall intensity. From this nearly linear relationship between Be and B band fluxes, they concluded that interpersed neutral gas within the LB must have an average density less than 0.025 cm^{-3} . Unfortunately, their sky coverage was limited and most of their viewpoints were not near any of our targets. An exception is WD 0501+527, for which $\log N(\text{H I}) = 18.11$ (Lemoine et al. 2002), and $d = 69 \text{ pc}$, which gives $\langle n(\text{H I}) \rangle = 0.007 \text{ cm}^{-3}$, below their limits. But only 30° away from one of the X-ray directions, toward WD 1631+781, the same calculation gives 0.1 cm^{-3} . It would be interesting to see if toward denser lines of sight (e.g., WD 0004+330 gives $\langle n(\text{H I}) \rangle = 0.24 \text{ cm}^{-3}$), there is measurable X-ray absorption in the lowest energy band.

We thank Cristina Oliveira, Guillaume Hébrard, Jean Dupuis, Martial André, Jeff Kruk, and Bill Oegerle for allowing us to use their results prior to publication and for enlightening discussions. We thank Jeff Linsky, Seth Redfield, and Barry Welsh for a careful reading of an earlier version and useful suggestions. This work is based on data obtained for the Guaranteed Time Team by the NASA-CNES-CSA FUSE mission operated by the Johns Hopkins University. Financial support to U. S. participants has been provided by NASA contract NAS5-32985. French participants are supported by CNES. This research has made use of the NASA Astrophysics Data System Abstract Service and the SIMBAD database, operated at CDS, Strasbourg, France.

REFERENCES

- Abgrall, H., Roueff, E., Launay, F., Roncin, J. Y., & Subtil, J. L. 1993a, *A&AS*, 101, 273
 Abgrall, H., Roueff, E., Launay, F., Roncin, J. Y., & Subtil, J. L. 1993b, *A&AS*, 101, 323
 Allende Prieto, C., Lambert, D. L., & Asplund, M. 2001, *ApJ*, 556, L63
 Anders, E., & Grevesse, N., 1989, *Geochim. Cosmochim. Acta*, 53, 197
 Andersson, B.-G., Idzi, R., Uomoto, A., Wannier, P. G., Chen, B., Jorgensen, A. M. 2002, *AJ*, 124, 2164
 André, M., et al. 2003a, *ApJ*, in press
 André, M., et al. 2003b, *ApJ*, in preparation
 Bannister, N. P., Barstow, M. A., Holberg, J. B., & Bruhweiler, F. C. 2003, *MNRAS*, 341, 477
 Bock, J. J., et al. 1993, *ApJ*, 410, L115
 Boulanger, F., et al. 1996, *ApJ*, 312, 256
 Bowyer, S., Drake, J. J., & Vennes, S. 2000, *ARA&A*, 38, 231
 Breitschwerdt, D., & Schmutzler, T. 1994, *Nature*, 371, 774
 Bruhweiler, F. C., & Kondo, Y., 1982, *ApJ*, 259, 232
 Cartledge, S. I. B. and Meyer, D. M. and Lauroesch, J. T., & Sofia, U. J. 2001, *ApJ*, 562, 394
 Chayer, P., Fontaine, G., & Wesemael, F. 1995, *ApJS*, 99, 189
 Chayer, P., Kruk, J. W., Ake, T. B., Dupree, A. K., Malina, R. F., Siegmund, O. H. W., Sonneborn, G., & Ohl, R. G. 2000, *ApJ*, 538, L91
 Dame, T. M., et al. 1987, *ApJ*, 322, 706
 Dupree, A. K., & Raymond, J. C. 1983, *ApJ*, 275, L71
 Dupuis, J., Vennes, S., Bowyer, S., Pradhan, A. K., & Thejll, P. 1995, *ApJ*, 455, 574
 Dupuis, J., et al. 2003, *ApJ*, in preparation
 Feldman, P. D., Sahnou, D. J., Kruk, J. W., Murphy, E. M., & Moos, H. W. 2001, *J. Geophys. Res.*, 106, 8119
 Ferlet, R. 1999, *A&A Rev.*, 9, 153
 Friedman, S. D., et al. 2002, *ApJS*, 140, 37
 Frisch, P. C., York, D. G. 1983, *ApJ*, 271, L59
 Frisch, P. C., Slavin, J. 1996, *Space Science Rev.*, 78, 223
 Frisch, P. C., et al. 1999, *ApJ*, 525, 492
 Génova, R., Molaro, P., Vladilo, G., & Beckman, J. E. 1990, *ApJ*, 355, 150
 Gry, C. 1996, *Space Sci. Rev.*, 78, 239
 Gry, C., Boulanger, F., Nehmé, C., Pineau des Forêts, Habart, E., & Falgarone, E. 2002, *A&A*, 391, 675
 Gry, C., & Jenkins, E. B. 2001, *A&A*, 367, 617
 Gry, C., Lequeux, J., & Boulanger, F. 1992, *A&A*, 266, 457
 Hébrard, G., et al. 2003a, *ApJ*, 140, 103
 Hébrard, G., et al. 2003, *ApJ*, in press
 Hobbs, L. M., Blitz, L., & Magnani, L. 1986, *ApJ*, 306, L109
 Hobbs, L. M., Blitz, L., Penrose, B. E., Magnani, L., & Welty, D. E. 1988, *ApJ*, 327, 356
 Holberg, J. B., Barstow, M. A., & Sion, E. M. 1998, *ApJ*, 119, 207
 Holberg, J. B., Saffer, R. A., Tweedy, R. W., & Barstow, M. A. 1995, *ApJ*, 452, L133
 Holmgren, D. E., Brown, P. J. F., Dufton, P. L., & Keenan, F. P. 1990, *ApJ*, 364, 657
 Holweber, H. 2001, in *Solar and Galactic composition*, ed. Wimmer-Schweingruber (Berlin: Springer).
 Hoopes, C. G., Sembach, K. R., Hébrard, G., Moos, H. W., & Knauth, D. C. 2003, *ApJ*, 586, 1094
 Howk, J. C., Sembach, K. R., Roth, K. C., & Kruk, J. W. 2000, *ApJ*, 544, 867
 Jenkins, E. B. 1986, *ApJ*, 304, 739
 Jenkins, E. B., et al. 2000, *ApJ*, 538, L81
 Juda, M., Bloch, J. J., Edwards, B. C., McCammon, D., Sanders, W. T., Snowden, S. L., & Zhang, J. 1991, *ApJ*, 367, 182.
 Keenan, F. P., Lennon, D. J., Johnson, C. T., & Kingston, A. E. 1986, *MNRAS*, 220, 571
 Keenan, F. P., Bates, B., Dufton, P. L., Holmgren, D. E., & Gilheany, S. 1990, *ApJ*, 348, 322
 Kruk, J. W., Chayer, P., & Dupuis, J. 2003, *Proc. 13th European Workshop on White Dwarfs*, ASP Conf. Series, R. Silvotti and D. DeMartino eds.
 Kruk, J. W., et al. 2002, *ApJS*, 140, 19
 Lallement, R., 1998, *Space Sci. Rev.*, 78, 361
 Lallement, R., 1998, *Lecture Notes in Physics*, 506, 19
 Lallement, R., Ferlet, R., Lagrange, A. M., Lemoine, M., & Vidal-Madjar, V. 1995, *A&A*, 304, 461
 Lehner, N., Gry, C., Sembach, K. R., Hébrard, G., Chayer, P., Moos, H. W., Howk, J. C., & Désert, J. M. 2002, *ApJS*, 140, 81
 Lemoine, M., et al. 2002, *ApJS*, 140, 67
 Linsky, J. L. 1996, *Space Sci. Rev.*, 78, 157
 Linsky, J. L., et al. 1993, *ApJ*, 402, 694
 Linsky, J. L., Redfield, S., Wood, B. E., & Piskunov, N. 2000, *ApJ*, 528, 756
 Luhman, K. L. 2001, *ApJ*, 560, 287
 Lyu, C., & Bruhweiler, F. C. 1996, *ApJ*, 459, 216
 Magnani, L., Blitz, L., & Mundy, L. 1985, *ApJ*, 295, 402
 McClintock, W., Henry, R. C., Moos, H. W., & Linsky, J. L. 1975, *ApJ*, 202, 733
 Meyer, D. M., Cardelli, J. A., & Sofia, U. J. 1997, *ApJ*, 490, L103
 Meyer, D. M., Jura, M., & Cardelli, J. A. 1998, *ApJ*, 493, 222
 Meyer, J.-P. 1989, in *Cosmic Abundances of Matter*, ed. C. J. Waddington, (New York: AIP), 245
 Moos, H. W., et al. 2000, *ApJ*, 538, L1
 Moos, H. W., et al. 2002, *ApJS*, 140, 3
 Morton, D. C. 1991, *ApJS*, 77, 119
 Oegerle, W.R., Jenkins, E.B., Shelton, R., Bowen, D.V., & Chayer, P., 2003, *ApJ*, submitted
 Oliveira, C., Hébrard, G., Howk, J. C., Kruk, J. W., Chayer, P., & Moos, H. W. 2003, *ApJ*, 587, 235
 Perryman, M. A. C., et al. 1997, *A&A*, 323, L49
 Redfield, S., & Linsky, J. L. 2000, *ApJ*, 534, 825
 Redfield, S., Linsky, J. L., Ake, T. B., Ayres, T. R., Dupree, A. K., Robinson, R. D., Wood, B. E., & Young, P. R. 2002, *ApJ*, 581, 626
 Redfield, S., & Linsky, J. L. 2003, *ApJ*, submitted
 Sahnou, D. J., et al. 2000, *ApJ*, 538, L7
 Savage, B. D., Bohlin, R. C., Drake J. F., & Budich, W. 1977, *ApJ*, 216, 291
 Savage, B. D., & Sembach, K. R. 1991, *ApJ*, 379, 245
 Savage, B. D., & Sembach, K. R. 1996a, *ARA&A*, 34, 279
 Savage, B. D., & Sembach, K. R. 1996b, *ApJ*, 470, 893
 Sembach, K. R., & Savage, B. D. 1992, *ApJS*, 83, 147
 Sfeir, D. M., Lallement, R., Crifo, F., & Welsh, B. Y. 1999, *A&A*, 346, 785
 Shull, J. M., & Van Steenberg, M. 1982, *ApJS*, 48, 95
 Slavin, J. D. 1989, *ApJ*, 346, 718
 Slavin, J. D., & Frisch, P. C. 1998, in the *Local Bubble and Beyond*, D. Breitschwerdt, M. J. Freyberg & J. Trümper (Eds.) (Springer: Berlin), p. 305
 Slavin, J. D., & Frisch, P. C. 2002, *ApJ*, 565, 364
 Sofia, U. J., & Jenkins, E. B. 1998, *ApJ*, 499, 951

Sofia, U. J., & Meyer, D. M. 2001, ApJ, 554, L221
 Sonneborn, G., et al. 2002, ApJS, 140, 51
 Spitzer, L., Cochran, W. D., & Hirshfeld, A. 1974, ApJS, 28, 373
 Spitzer, L., Drake, J. F., Jenkins, E. B., Morton, D. C., Rogerson, J. B., & York, D. G. 1973, ApJS, 181, L116
 Tat, H. H., & Terzian, Y. 1999, PASP, 111, 1258
 Trapero, J., Sempere, M. J., Beckman, J. E., Hobbs, L. M. 1996, ApJ, 457, 731
 Vallerger, J. V. 1998, ApJ, 497, 921
 Vallerger, J. V., Vedder, P. W., Craig, N., & Welsh, B. Y. 1993, ApJ, 411, 729
 Vennes, S., Dupuis, J., Chayer, P., Polomski, E. F., Dixon, W. V. D., & Hurwitz, M. 1998, ApJ, 500, L41
 Vennes, S., Thejll, P. A., Galvan, R. G., & Dupuis, J. 1997, ApJ, 480, 714
 Vidal-Madjar, A., et al. 1998 A&A, 338, 694
 Welsh, B. Y.; Sfeir, D. M., Sirk, M. M., & Lallement, R. 1999, A&A, 353, 308
 Welty, D. E., Hobbs, L. M., Lauroesch, J. T., Morton, D. C., Spitzer, L., & York, D. G. 1999, ApJS, 124, 465
 Wiese, L. M., Bonvallet, G. A., & Lawler, J. E. 2002, ApJ, 569, 1032
 Wolff, B., Koester, D., & Lallement, R. 1999, A&A, 329, 1045
 Wood, B. E., & Linsky, J. L. 1997, ApJ, 474, L39
 Wood, B. E., et al. 2002a, ApJS, 140, 91
 Wood, B. E., Redfield, S., Linsky, J. L., & Sahu, M. S. 2002b, ApJ, 581, 1168

TABLE 1
 SIGHTLINE SUMMARY

WD name	Other name	l ($^{\circ}$)	b ($^{\circ}$)	v_{helio} (km s^{-1})	d (pc)	Spectral Type	Aperture	Notes
WD 0004+330	GD 2	112.48	-28.69	+0.1	97 ^a	DA	LWRS, MDRS	[A] (1)
WD 0050-332	GD 659	299.15	-84.12	+12.2	58 ^a	DA1	LWRS	[B] (2)
WD 0131-163	GD 984	167.26	-75.15	...	96 ^a	DA1	LWRS	[B] (2)
WD 0455-282	MCT 0455-2812	229.29	-36.17	+13.6	102 ^a	DA1	MDRS	[C] (2)
WD 0501+527	G191-B2B	155.95	+7.10	+13.0	69 ± 16 (59 ^a)	DA1	LWRS, MDRS, HIRS	[C] (3)
WD 0549+158	GD 71	192.03	-5.34	+23.2	49 ^a	DA1	LWRS	[A] (2)
WD 0621-376		245.41	-21.43	+19.5	78 ^a	DA	LWRS, MDRS	[D] (4)
WD 0715-703		281.62	-23.50	...	94 ^a	DA1	MDRS	[A] (2)
WD 1017-138		255.74	+34.53	+34.5	90 ^a	DA	LWRS	[A] (2)
WD 1202+608	GD 314, Feige 55	133.11	+55.66	-16.1	200 ^d	DA	MDRS	[C] (2)
WD 1211+332	HZ 21	175.03	+80.02	-18.0	115 ± 35	DO	LWRS, MDRS	[B] (5)
WD 1234+481		129.81	+69.01	-28.9	129 ^a	DA	LWRS	[A] (2)
WD 1254+223	GD 153	317.26	+84.75	-11.1	67 ^a	DA1	LWRS	[A] (2)
WD 1314+293	HZ 43	54.10	+84.16	-17.4	68 ± 13	DA1	LWRS, MDRS	[A] (6)
WD 1528+487		78.87	+52.72	...	140 ^a	DA:	LWRS	[B] (2)
WD 1615-154	EGGR 118	358.79	+24.18	-38.2	55 ^d	DA1.5	MDRS	[A] (2)
WD 1631+781	1ES 1631+78.1	111.29	+33.58	-11.8	67 ^a	DA1	MDRS	[A] (7)
WD 1634-573	HD 149499 B	329.88	-7.02	-19.6 ^α	37 ± 3	DOZ1	LWRS, MDRS	[B] (8)
WD 1636+351		56.98	+41.40	...	109 ^a	DA	LWRS	[A] (2)
WD 1800+685		98.73	+29.78	-15.9	159 ^a	DA1	MDRS	[A] (2)
WD 1844-223		12.50	-9.25	...	62 ^a	DA:	LWRS	[A] (2)
WD 2004-605		336.58	-32.86	-28.0	58 ^a	DA	MDRS	[A] (7)
WD 2011+395	EUVE J2013+40.0	77.00	+3.18	...	141 ^a	DAO	LWRS	[B] (2)
WD 2111+498	GD 394	91.37	+1.13	-6.2	50 ^a	DA2	LWRS	[B] (2)
WD 2124-224		26.81	-43.19	...	224 ^b	DA	MDRS	[B] (2)
WD 2148+286*	BD+28° 4211	81.87	-19.29	-20.2 ^β	104 ± 18	SdO	LWRS, MDRS	[E] (9)
WD 2152-548		339.73	-48.06	...	128 ^a	DA:	MDRS	[A] (2)
WD 2211-495		345.79	-52.62	-0.7	53 ^a	DA	LWRS, MDRS, HIRS	[D] (10)
WD 2247+583	Lan 23	107.64	-0.64	...	122 ^a	DA	LWRS	[C] (5)
WD 2309+105	GD 246	87.26	-45.11	-7.9	79 ^a	DA1	LWRS, MDRS	[B] (5)
WD 2331-475	MCT 2331-4731	334.83	-64.81	+14.9	82 ^a	DA	LWRS, MDRS	[B] (5)

Note. — Heliocentric velocities are from Holberg, Barstow, & Sion (1998), except (α) from Wood et al. (2002a) and (β) from Sonneborn et al. (2002). *Note that using the denomination WD 2148+286 for BD+28° 4211 is somewhat incorrect because this star is a subdwarf of type O, not a white dwarf. However, for consistency and simplicity, we have used this name throughout the article. *a*: Distances from Vennes et al. (1997). *b*: Distance from Vennes et al. (1998). *c*: Distance from Dupuis (2002, private communication). *d*: Distances from Holberg, Barstow, & Sion (1998). Distances with errors are from Hipparcos parallax measurements (Perryman et al. 1997); for the others, the errors are typically 20–30%. Metallicity of the star: [A] no metal detected in *FUSE* spectra; [B] few metals; [C] rich in metals; [D] very rich in metals; [E] solar metallicity (see Dupuis et al. 2003, in preparation, and references below). Source of the column densities: (1) Oliveira et al. (2003, private communication), this work; (2) this work; (3) Lemoine et al. (2002); André et al. (2003b); (4) Lehner et al. (2002), this work; (5) Oliveira et al. (2003), this work; (6) Kruk et al. (2002); (7) Hébrard et al. (2003), this work; (8) Wood et al. (2002a), this work; (9) Sonneborn et al. (2002), this work; (10) Hébrard et al. (2003), this work.

TABLE 2
ATOMIC DATA USED IN THIS WORK

Ions	λ_{lab} (Å)	f	Note
C II	1036.337	1.18×10^{-1}	saturated (a)
C II*	1037.018	1.18×10^{-1}	
C III	977.020	7.58×10^{-1}	blended (b)
N I	952.303	1.70×10^{-3}	
	952.415	1.87×10^{-3}	
	953.415	1.32×10^{-2}	
	953.655	2.50×10^{-2}	
	953.970	3.48×10^{-2}	
	963.990	1.48×10^{-2}	
	964.626	9.43×10^{-3}	
	965.041	4.02×10^{-3}	
	1134.165	1.52×10^{-2}	airglow (c)
	1134.415	2.97×10^{-2}	airglow (c)
	1134.980	4.35×10^{-2}	airglow (c)
N II	1083.994	1.15×10^{-1}	saturated (a)
O I	919.658	9.48×10^{-4}	
	919.917	1.78×10^{-4}	
	921.857	1.19×10^{-3}	
	922.200	2.45×10^{-4}	
	924.950	1.54×10^{-3}	
	925.446	3.50×10^{-4}	
	929.517	2.29×10^{-3}	
	930.257	5.37×10^{-4}	
	936.630	3.65×10^{-3}	
	948.686	6.31×10^{-3}	
	950.885	1.58×10^{-3}	
	976.448	3.31×10^{-3}	
	1039.230	9.20×10^{-3}	airglow (c)
Si II	1020.699	1.64×10^{-2}	
Ar I	1048.220	2.63×10^{-1}	
	1066.660	6.75×10^{-2}	blended (d)
P II	1152.818	2.45×10^{-1}	
Fe II	1055.262	7.50×10^{-3}	
	1063.176	5.47×10^{-2}	
	1096.877	3.20×10^{-2}	
	1125.448	1.60×10^{-2}	
	1143.226	1.77×10^{-2}	
	1144.938	1.06×10^{-1}	
Fe III	1122.524	5.44×10^{-2}	

Note. — Rest frame vacuum wavelengths and oscillator strengths are from Morton (private communication, 2000), except for the f -values of Fe II which are from Howk et al. (2000). (a) These lines are generally strong and usually only a lower limit can be estimated (except in few cases where the column densities are extremely small). (b) Interstellar C III can be blended with the stellar component if the star contains some metals. (c) Those lines can be affected by airglow emission lines, especially the N I triplet. (d) Ar I λ 1066 can be blended with stellar Si IV λ 1066 if the star contains some metals.

TABLE 3
COMPARISON OF O I AND N I b -VALUES

Sightline	b [O I] (km s ⁻¹)	b [N I] (km s ⁻¹)
WD 0004+330	6.3 ± 0.3	4.8 ± 0.4
WD 0050-332	5.3 ± 0.4	5.3 :
WD 0131-163	5.5 ± 0.6	5.5 :
WD 0455-282	5.8 ± 0.2	...
WD 0715-703	5.8 ± 0.5	...
WD 1017-138	6.4 ± 0.3	6.2 ± 0.5
WD 1202+608	5.7 ± 0.9	6.2 ± 1.1
WD 1234+481	5.4 ± 1.0	4.8 ± 0.5
WD 1528+487	5.4 ± 0.3	4.8 ± 0.3
WD 1615-154	5.0 ± 0.2	5.0 :
WD 1631+781	5.8 ± 0.4	6.3 ± 0.3
WD 1636+351	4.3 :	4.3 ± 0.3
WD 1800+685	6.4 ± 0.3	4.7 ± 0.2
WD 1844-223	6.1 ± 0.4	4.7 ± 0.3
WD 2004-605	6.1 ± 1.5	5.7 ± 1.0
WD 2111+498	8.4 ± 0.5	8.8 ± 0.3
WD 2124-224	4.5 ± 0.6	4.3 ± 0.2
WD 2152-548	4.3 ± 0.3	4.3 ± 0.7
WD 2331-475	4.3 ± 0.2	4.5 ± 0.4
	8.0 ± 1.6	7.9 ± 1.5
	10.7 ± 0.2	10.7 ± 1.0
	5.0 ± 0.3	5.4 ± 0.9
	8.6 ± 0.4	7.8 ± 0.6
	8.6 ± 0.3	7.8 ± 0.7

Note. — “:” means that the b -value was taken from the other species; see text.

TABLE 4
COLUMN DENSITY SUMMARY

Star	C II	C II*	C III	O I	N I	N II	Si II	Ar I	Fe II	Fe III	P II
WD 0004+330	>14.38	>13.51	>13.40	16.20 16.35 16.50	15.15 15.30 15.45	>14.12	>14.34	>13.80	13.55 13.60 13.68	<12.95	12.83 12.85 12.87
WD 0050-332	>14.09	12.29 12.55 12.71	<13.14	15.21 15.26 15.32	14.01 14.30 14.60	>13.91	<13.60	<12.67	12.80 13.06 13.22	...	<12.39
WD 0131-163	>14.20	12.84 13.00 13.12	<13.27	15.83 15.89 15.97	14.80 14.91 15.04	>14.11	13.80 13.93 14.05	12.90 12.97 13.03	13.51 13.54 13.57	...	12.66 12.78 12.87
WD 0455-282a	13.54 13.58 13.62	<12.68	<12.66	<14.12	<13.13	<13.47	<12.88	<12.62	<12.73	...	<12.39
WD 0455-282b	>14.20	12.46 12.68 12.83	>13.72	14.91: 14.86 13.59	13.29 13.44 13.59	>13.92	13.34:	<12.62	12.83 12.94 13.02	<12.99	<12.39
WD 0501+527	>15.39	13.23 13.26 13.28	...	14.82 14.86 14.90	13.83 13.87 13.91	>13.83	13.51 13.52 13.53	<12.00	13.03 13.05 13.07	...	<11.85
WD 0549+158	13.79 13.81 13.84	<12.84	12.59 12.72 12.81	14.18 14.27 14.34	<13.60	13.43 13.49 13.54	12.75 12.99 13.14	<12.46	<12.64	<13.12	<12.23
WD 0621-376	>14.19	13.04 13.09 13.14	<13.31	15.22 15.26 15.31	14.27 14.34 14.41	>13.80	<13.68	12.79 12.86 12.93	12.79 12.94 13.05
WD 0715-703	>14.29	13.31 13.42 13.51	>13.22	15.81 15.90 16.00	14.89 14.96 15.04	>14.00	13.97 14.09 14.18	13.09 13.17 13.25	13.52 13.56 13.61	<13.34	11.76 12.25 12.47
WD 1017-138	>14.10	12.93 13.10 13.23	13.05 13.14 13.21	15.73 15.95 16.40	14.46 14.55 14.64	>13.90	13.90 14.06 14.17	13.02 13.17 13.28	13.55 13.60 13.65	...	12.18 12.23 12.57
WD 1202+608a	>14.83	12.28 12.60 12.78	>14.14	14.57 14.70 14.84	13.12 13.37 13.42	>14.38	14.05 14.11 14.17	11.88 12.18 12.55	13.68 13.72 13.77
WD 1202+608b	>14.65	12.94 13.07 13.17	>14.14	15.63 15.65 15.68	14.75 14.77 14.79	>14.10	14.13 14.19 14.25	12.90 13.07 13.19	13.70 13.74 13.78
WD 1211+332	>14.39	13.07 13.14 13.19	>13.49	15.69 15.74 15.79	14.73 14.77 14.81	>14.03	14.32 14.36 14.40	13.13 13.16 13.19	13.50 13.54 13.58	<13.43	12.50 12.57 12.63
WD 1234+481	>14.23	12.74 12.89 13.01	>13.60	15.56 15.63 15.71	14.58 14.62 14.67	>14.15	13.65 13.87 14.01	12.83 12.90 12.96	12.92 13.07 13.19	...	12.14 12.48 12.66
WD 1254+223	13.62 13.64 13.66	<12.66	12.20:	14.26 14.38 14.58	13.25 13.30 13.45	12.96 13.07 13.16	<12.69	11.71 12.04 12.23	<12.54	<12.94	<12.30
WD 1314+293	14.66 14.83 14.92	<12.73	12.54 12.59 12.64	14.48 14.51 14.54	13.48 13.51 13.54	13.54 13.62 13.69	12.74 12.85 12.94	11.71 11.96 12.11	12.15 12.17 12.19	<12.64	<11.97
WD 1528+487a	13.26 13.32 13.36	<12.88	>13.55:	<14.07	<13.46	<13.22	<13.04	<12.55	<13.22	<13.30	<12.56
WD 1528+487b	>14.23	12.89 12.99 13.05	>13.55:	15.72 15.80 15.88	14.95 14.99 15.04	>14.03	13.80 13.91 14.01	13.42 13.46 13.49	13.24 13.36 13.45	<13.30	12.10 12.40 12.70
WD 1615-154	>14.03	13.08 13.17 13.25	12.78 12.96 13.09	15.68 15.78 15.89	14.93 15.03 15.18	13.61 13.71 13.79	<13.94	13.27 13.29 13.31	13.44 13.50 13.57	<13.16	12.39 12.45 12.59
WD 1631+781	>14.32	13.02 13.17 13.32	>13.41	15.81 15.90 15.99	15.18 15.28 15.38	>14.12	14.01 14.11 14.21	13.45 13.53 13.61	13.20 13.23 13.26	<12.68	12.59 12.71 12.83
	15.65			15.48	14.58	14.72	13.59	13.20	13.01		12.01

TABLE 4—Continued

Star	C II	C II*	C III	O I	N I	N II	Si II	Ar I	Fe II	Fe III	P II
WD 1634–573	15.90 16.25	...	<15.4	15.51 15.54	14.62 14.66	14.90 15.08	13.76 13.89	13.26 13.32	13.08 13.15	...	12.08 12.15
WD 1636+351	>14.25	13.23 13.34 13.44	>13.27	15.58 15.71 15.95	>15.08	>14.08	14.15 14.30 14.42	13.64 13.70 13.76	13.94 13.98 14.02	<13.41	12.70 12.75 12.80
WD 1800+685	>14.47	13.57 13.63 13.67	>13.56	16.02 16.12 16.26	15.02 15.05 15.09	>14.21	14.44 14.53 14.60	13.81 13.83 13.93	13.87 13.97 14.07	12.14 12.80 13.05	12.80 12.94 13.05
WD 1844–223	>14.16	12.87 13.04 13.16	>13.25	15.85 15.97 16.15	14.91 15.06 15.36	>13.82	14.28 14.38 14.45	13.54 13.58 13.62	13.42 13.53 13.66	<13.11	12.45 12.59 12.69
WD 2004–605	>14.02	12.81 12.99 13.17	13.12 13.15 13.17	15.57 15.65 15.73	14.76 14.84 14.92	>13.85	13.92 14.07 14.22	13.18 13.26 13.34	13.18 13.25 13.32	<12.90	12.30 12.37 12.44
WD 2011+395	>14.39	13.35 13.38 13.41	<13.48	16.01 16.06 16.12	15.20 15.48 15.61	>14.34	14.16 14.23 14.29	13.40 13.43 13.93	13.69 13.72 13.75	<14.09	12.39 12.59 12.72
WD 2111+498	>14.12	13.05 13.12 13.18	<13.00	15.00 15.06 15.11	13.97 14.00 14.08	>13.91	13.31 13.35 13.31	12.46 12.58 12.68	13.29 13.23 13.35	...	<12.47
WD 2124–224	>14.57	13.41 13.47 13.52	>13.75	15.91 15.94 15.97	14.93 14.97 15.04	>14.32	14.44 14.49 14.53	13.50 13.57 13.64	14.18 14.22 14.27	...	12.62 12.74 12.83
WD 2148+286	>14.43	13.73 13.75 13.76	>13.54	16.17 16.22 16.27	15.48 15.55 15.62	>14.13	...	>13.60
WD 2152–548	>14.30	12.65 12.95 13.13	>13.37	15.42 15.49 15.59	14.37 14.42 14.48	>14.12	13.38 13.76 13.97	12.56 12.72 12.90	13.34 13.37 13.40	<13.23	<12.84
WD 2211–495	>14.34	12.79 12.88 12.96	>13.58	15.31 15.34 15.38	14.27 14.30 14.33	14.45 14.60 14.75	13.92 14.00 14.08	12.77 12.82 12.87	13.17 13.25 13.33	...	11.95 12.05 12.15
WD 2247+583	>14.41	13.56 13.59 13.63	>13.31	16.53 16.72 16.87	15.66 15.73 15.80	>13.95	> 14.52	> 13.50	13.96 14.03 14.10	<13.14	...
WD 2309+105	>14.20	13.05 13.08 13.10	>13.37	15.63 15.67 15.71	14.72 14.75 14.78	>13.81	14.05 14.07 14.10	13.09 13.14 13.21	13.25 13.30 13.35	...	12.24 12.29 12.34
WD 2331–475	>14.43	13.18 13.27 13.36	>13.60	15.42 15.48 15.54	14.48 14.53 14.58	>14.27	13.89 13.99 14.09	12.67 12.77 13.87	13.27 13.32 13.37	...	12.08 12.18 12.28

Note. — For a given sightline and a given species, there are 3 entries: the second number corresponds to the most likely value, while the first and third correspond to -1σ and $+1\sigma$, respectively. < indicates a 3σ upper limit detection, except in the case of C III where the upper limit reflects that this line may be blended with the C III photospheric lines. > indicates a lower limit, i.e. the line is saturated. Colon means that the value is uncertain. See § 3 and Table 1 for more details and references, respectively. Two entries for one sightline (denoted by a and b) indicate that two components are detected with FUSE: for WD 0455–282, component a is at -58 km s^{-1} and b at -2 km s^{-1} ; for WD 1202+608, component a is at -58 km s^{-1} and b at -2 km s^{-1} ; and for WD 1528+487, component a is at -56 km s^{-1} and b at -16 km s^{-1} .

TABLE 5
H₂ MEASUREMENTS

Sightline	$N_{J=0}$	$N_{J=1}$	$N_{J=2}$	$N_{J=3}$	N_{all}	b (km s^{-1})	T_{ex} (K)
WD 0004+330	13.45 ± 0.06 (1)	14.35 ± 0.04 (22)	13.71 ± 0.04 (10)	13.52 ± 0.07 (4)	14.46	3.8 ± 0.7	314 ± 42^a
WD 1636+351	14.21 ± 0.20 (7)	14.83 ± 0.07 (25)	14.30 ± 0.15 (13)	14.04 ± 0.10 (3)	15.05	3.1 ± 0.2	314 ± 31
WD 1800+685	14.02 ± 0.26 (5)	14.49 ± 0.15 (12)	14.00 ± 0.10 (12)	13.79 ± 0.18 (1)	14.75	5.0 ± 4.2	301 ± 38
WD 2011+395	...	14.55 ± 0.10 (13)	14.05 ± 0.20 (2)	13.83 ± 0.20 (2)	14.22	2.8 ± 0.3	349 ± 74
WD 2148+286	14.32 ± 0.11 (4)	15.25 ± 0.24 (8)	14.34 ± 0.15 (13)	14.18 ± 0.14 (14)	15.38	3.0 ± 0.6	297 ± 35
WD 2247+583	14.24 ± 0.03 (6)	14.94 ± 0.04 (13)	14.23 ± 0.03 (14)	13.94 ± 0.04 (7)	15.11	4.1 ± 0.4	276 ± 8

Note. — The number of lines used to measure the column density is shown in parentheses. For WD 0004+330, WD 2148+286, and WD 2247+583, the column densities and b -values are from Oliveira et al. (2003, private communication) Sonneborn et al. (2003, erratum in preparation), and Oliveira et al. (2003), respectively. a : For WD 0004+330, only the J -levels 1, 2, 3 could be fitted in the temperature relation within 1σ error bar, $T_{01} \approx 1363 \text{ K}$.

TABLE 6
[Ar I/O I], [N I/O I], AND N I/(N II + N I) RATIOS

Sightlines	[Ar I/O I]	[N I/O I]	N I/(N II+N I)
WD 0004+330	> -0.41	-0.29 ± ^{0.20} _{0.23}	< 0.94
WD 0050-332	< -0.45	-0.20 ± ^{0.30} _{0.30}	< 0.71
WD 0131-163	-0.78 ± ^{0.10} _{0.10}	-0.22 ± ^{0.15} _{0.13}	< 0.86
WD 0455-282b	< -0.15	-0.71 :	< 0.25
WD 0501+527	< -0.72	-0.23 ± ^{0.06} _{0.06}	< 0.52
WD 0549+158	< 0.33	< 0.09	0.56 :
WD 0621-376	-0.26 ± ^{0.08} _{0.08}	-0.16 ± ^{0.08} _{0.08}	< 0.77
WD 0715-703	-0.59 ± ^{0.13} _{0.13}	-0.18 ± ^{0.12} _{0.12}	< 0.90
WD 1017-138	-0.64 ± ^{0.45} _{0.30}	-0.64 ± ^{0.45} _{0.23}	< 0.82
WD 1202+608a	-0.38 ± ^{0.36} _{0.36}	-0.57 ± ^{0.31} _{0.31}	< 0.09
WD 1202+608b	-0.44 ± ^{0.12} _{0.17}	-0.12 ± ^{0.04} _{0.03}	< 0.82
WD 1211+332	-0.44 ± ^{0.06} _{0.06}	-0.21 ± ^{0.06} _{0.06}	< 0.85
WD 1234+481	-0.59 ± ^{0.10} _{0.10}	-0.25 ± ^{0.09} _{0.08}	< 0.75
WD 1254+223	-0.20 ± ^{0.38} _{0.38}	-0.32 ± ^{0.13} _{0.13}	0.63 ± ^{0.10} _{0.02}
WD 1314+293	-0.41 ± ^{0.15} _{0.25}	-0.24 ± ^{0.04} _{0.04}	0.44 ± ^{0.03} _{0.03}
WD 1528+487b	-0.20 ± ^{0.07} _{0.11}	-0.05 ± ^{0.08} _{0.11}	< 0.90
WD 1615-154	-0.35 ± ^{0.10} _{0.10}	0.01 ± ^{0.15} _{0.15}	0.95 ± ^{0.08} _{0.04}
WD 1631+781	-0.23 ± ^{0.12} _{0.12}	0.14 ± ^{0.13} _{0.13}	< 0.94
WD 1634-573	-0.11 ± ^{0.13} _{0.07}	-0.13 ± ^{0.05} _{0.05}	0.34 ± ^{0.13} _{0.09}
WD 1636+351	0.13 ± ^{0.24} _{0.15}	> 0.13	< 0.91
WD 1800+685	-0.15 ± ^{0.16} _{0.10}	-0.31 ± ^{0.14} _{0.11}	< 0.87
WD 1844-223	-0.25 ± ^{0.18} _{0.13}	-0.15 ± ^{0.33} _{0.21}	< 0.94
WD 2004-605	-0.25 ± ^{0.12} _{0.12}	-0.05 ± ^{0.12} _{0.12}	< 0.91
WD 2011+395	-0.48 ± ^{0.50} _{0.06}	0.19 ± ^{0.17} _{0.29}	< 0.93
WD 2111+498	-0.34 ± ^{0.11} _{0.14}	-0.30 ± ^{0.09} _{0.07}	< 0.55
WD 2124-224	-0.23 ± ^{0.08} _{0.04}	-0.20 ± ^{0.08} _{0.05}	< 0.82
WD 2148+286	> -0.48	0.09 ± ^{0.08} _{0.09}	< 0.96
WD 2152-548	-0.63 ± ^{0.20} _{0.18}	-0.31 ± ^{0.11} _{0.09}	< 0.67
WD 2211-495	-0.38 ± ^{0.06} _{0.07}	-0.28 ± ^{0.05} _{0.03}	0.33 ± ^{0.08} _{0.06}
WD 2247+583	-0.65 ± ^{0.21} _{0.19}	-0.23 ± ^{0.13} _{0.21}	< 0.98
WD 2309+105	-0.39 ± ^{0.10} _{0.10}	-0.16 ± ^{0.05} _{0.05}	< 0.89
WD 2331-475	-0.64 ± ^{0.07} _{0.10}	-0.31 ± ^{0.07} _{0.06}	< 0.63

Note. — Suffix “a” after star names means it is a high velocity component (see § 9), while “b” means that it is the low velocity component. Colon means that the value is uncertain.

TABLE 7
C III/C II RATIO

Targets	log[N(C III)/N(C II)]	log[N(C III)/N(C II)] _c	Note
WD 0050-332	< -0.95	< -1.26 to < -0.95	C II LL, C III SC?
WD 0131-163	< -0.93	< -0.93	C II LL
WD 0455-282a	< -0.92	...	C III UL
WD 0549+158	-1.09	< -1.09 to < -1.05	C III SC?
WD 0621-376	< -0.90	< -1.05	C II LL, C III SC
WD 1017-138	< -0.96	< -0.96	C II LL
WD 1254+223	-1.44 :	< -1.44 :	C III SC?
WD 1314+293	-2.24	-2.39 to -2.24	C III SC?
WD 1528+487a	> 0.23 :	...	C III LL
WD 1615-154	< -1.07	< -1.07	C II LL
WD 1634-573	< -0.50	-0.63	C III SC
WD 2004-605	< -0.87	< -0.87	C II LL
WD 2011+395	< -0.91	< -1.44	C II LL, C III SC
WD 2111+498	< -1.12	< -1.52	C II LL, C III SC

Note. — The second column presents the raw measurement, while the third one includes possible stellar correction for C III. When two numbers are indicated in the third column, it means that only an upper limit was derived for the amount of photospheric C III λ 977. LL: lower limit. UL: upper limit. SC: C III stellar contamination. SC?: possible C III stellar contamination. Suffix “a” after star names means the ratio is for a high velocity component (see § 9), and this component is not blended with any stellar lines. Colon means that the value is uncertain.

TABLE 8
 FE III/FE II RATIO

Targets	$\log[N(\text{Fe III})/N(\text{Fe II})]$
WD 0004+330	< -0.65
WD 0455-282b	< 0.05
WD 0715-703	< -0.22
WD 1211+332	< -0.11
WD 1314+293	< 0.47
WD 1528+487b	< -0.06
WD 1615-154	< -0.34
WD 1631+781	< -0.63
WD 1636+351	< -0.57
WD 1800+685	-1.17 :
WD 1844-223	< -0.42
WD 2004-605	< -0.35
WD 2011+395	< 0.37
WD 2152-548	< -0.14
WD 2247+583	< -0.89

Note. — Here “ $<$ ” is a 3σ upper limit.
 Colon means that the value is uncertain.

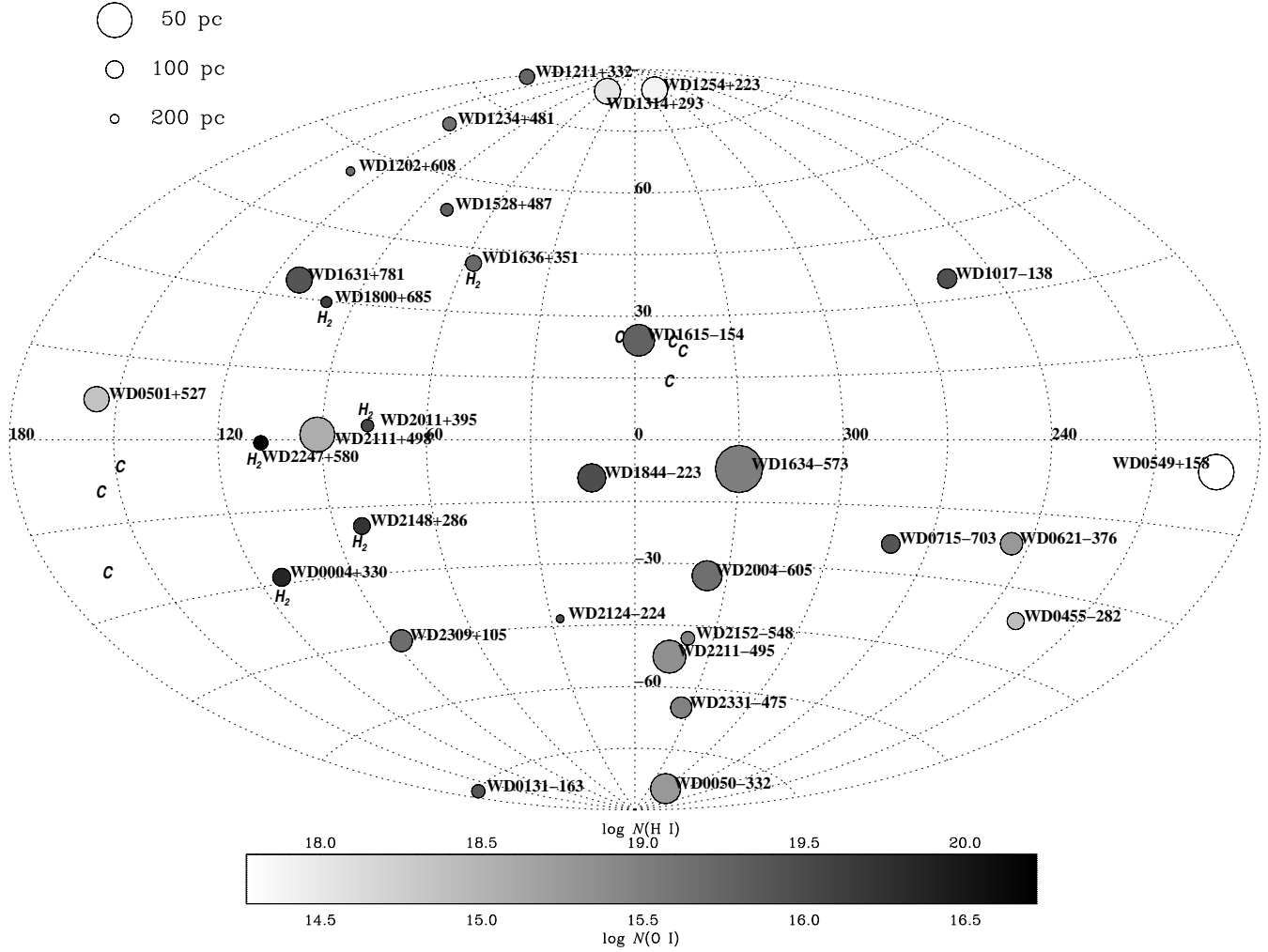


FIG. 1.— Target locations and the total O I column densities in Galactic coordinates (l, b). The diameter of each circle is inversely proportional to the distance of the line of sight, and the shading of the symbol indicates the total column density. The H I values were computed from the O I values using the O I/H I ratio discussed in the text. We indicate the presence of molecular hydrogen by the symbol H_2 for detection by this survey and “C” for sightlines near WD 1615–154 and $l \sim 150^\circ$ from the survey of Spitzer, Cochran, & Hirshfeld (1974) based on *Copernicus* data (the stars in the *Copernicus* study are between 111 and 166 pc).

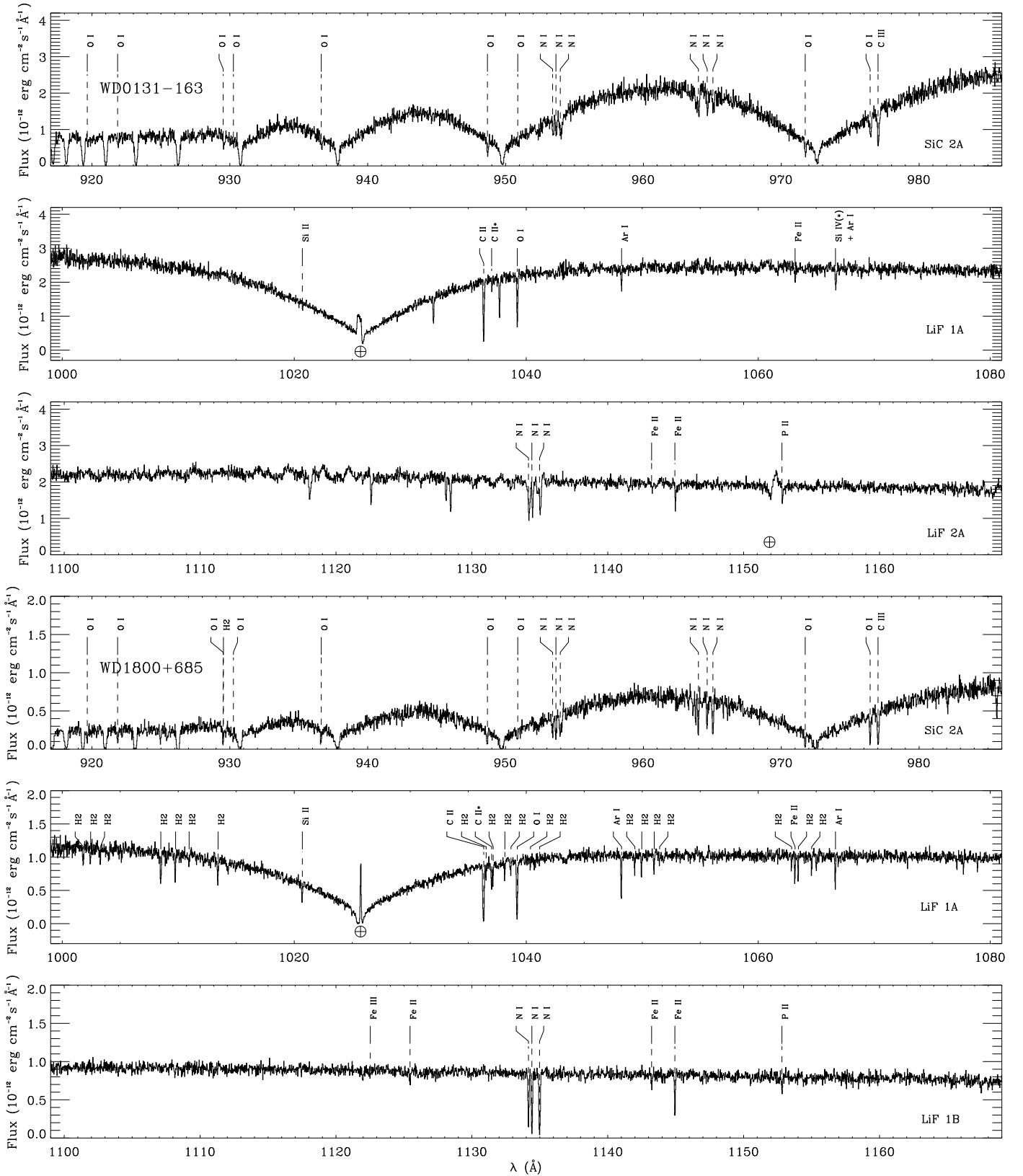


FIG. 2.— Two examples of *FUSE* WD spectra, with WD 0131–163 shown in top three panels and WD 1800+685 in bottom three panels. WD 1800+685 is a pure hydrogen WD with no photospheric metal absorption lines, but shows absorption by interstellar atoms, ions, and H₂. WD 0131–163 has a few stellar lines (note in particular the stellar Si IV blended with Ar I at 1066.66 Å). The positions of strong airglow emission lines are indicated by the earth symbol.

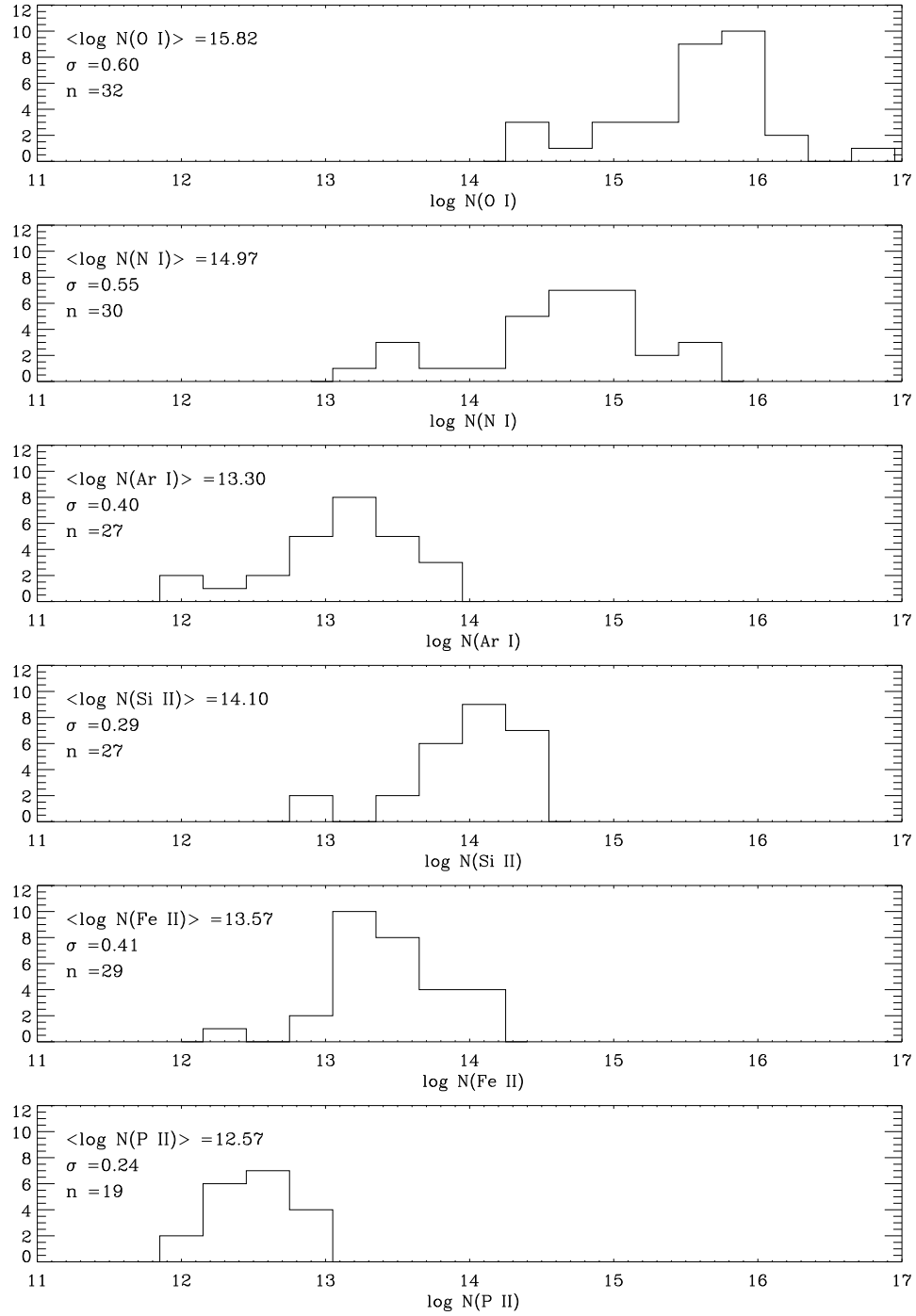


FIG. 3.— Histograms of column densities for the different ions observed. The mean, standard deviation and number of detected clouds (n) are listed in the upper-left of each plot.

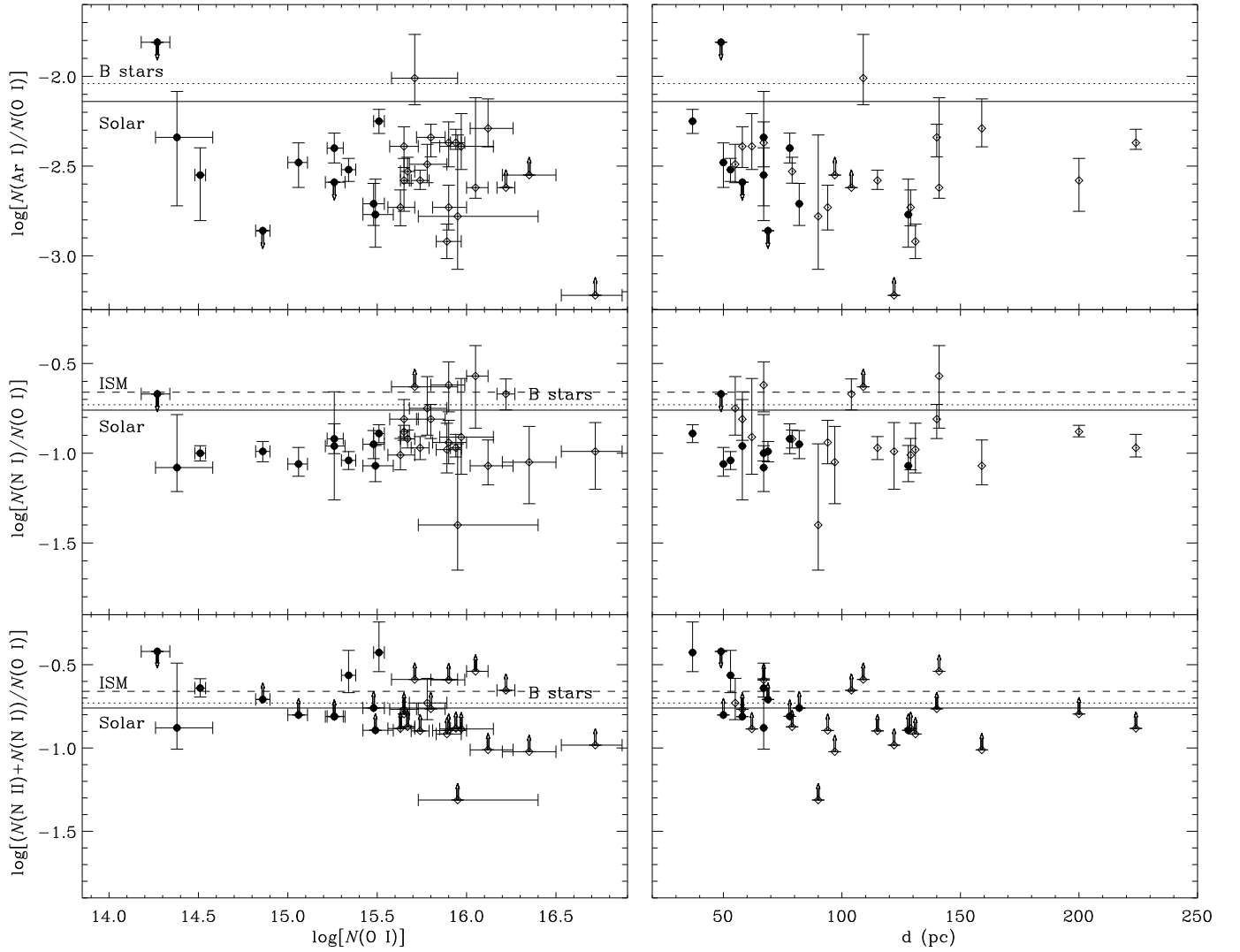


FIG. 4.— Logarithmic ratios of Ar I, N I, and (N I + N II)/O I plotted versus the total O I column density and the distance of the sightlines (note that the distance is only an upper limit to the interstellar clouds). The horizontal lines indicate the solar, B-type star, and interstellar values. The Local Bubble ($\log N(\text{O I}) \lesssim 15.60$) data points are shown with filled circles.

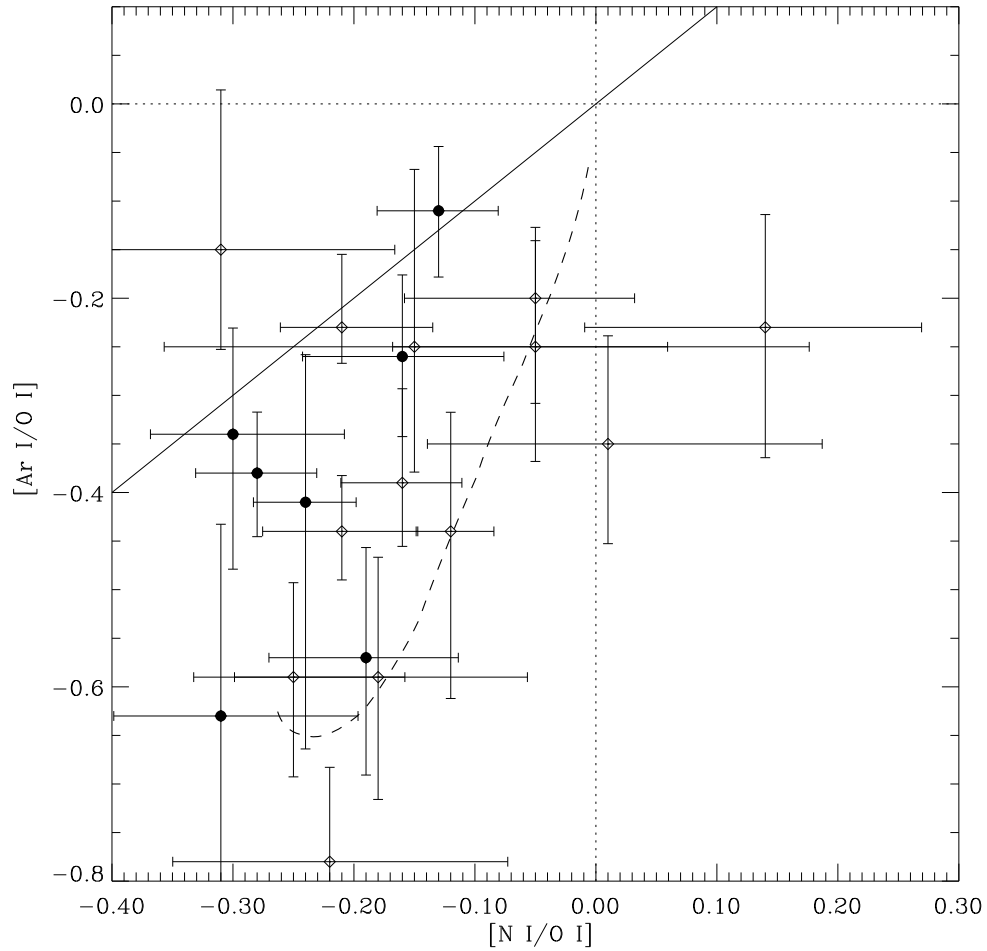


FIG. 5.— Logarithmic ratio of Ar I/O I plotted versus N I/O I. Both ratios are normalized to their solar values. The straight continuous line shows a 1:1 relationship. The dashed lines present the expected deficiency of Ar I and N I from a photoionization model (see § 6.3 and Figure 6). The Local Bubble ($\log N(O\ I) \lesssim 15.60$) data points are shown with filled circles.

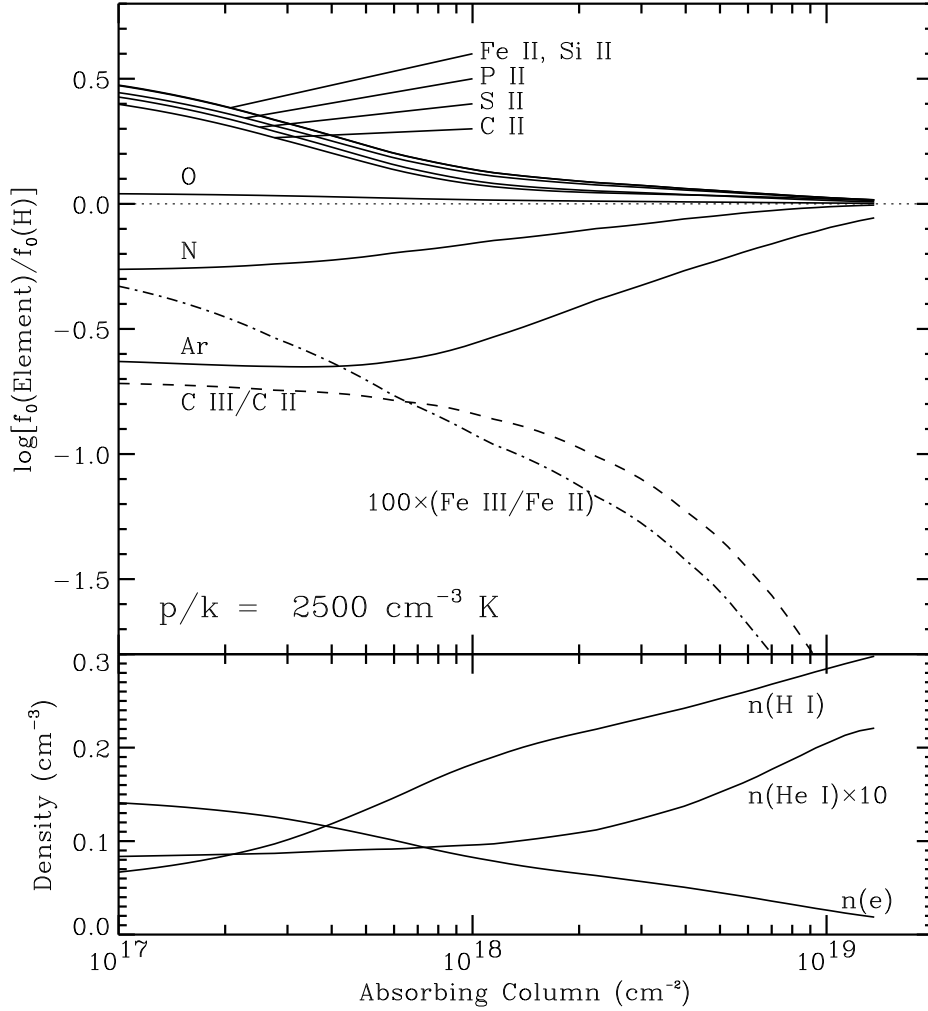


FIG. 6.— Results from a photoionization model of gas in the LB. *Top*: Logarithms of the expected deficiencies in the neutral fractions of $f_0 = n(\text{neutral})/n(\text{total})$ of N, O, and Ar compared to those of H (see 6.3 for more details). Also plotted are the logarithms of $n(X^+)/n(\text{total})$, i.e the singly ionized species, compared to the neutral fraction of H, along with the ratios C III/C II and Fe III/Fe II (using the same logarithmic scale on the vertical axes). All the calculations assume the same ionizing radiation field and include the effects of charge exchange with neutral hydrogen. These fractions are plotted as a function of absorbing column and hence shielding depth scaled to $N(\text{H I})$ for a cloud of uniform pressure p/k . *Bottom*: Densities of neutral hydrogen, neutral helium, and electrons against shielding depth.

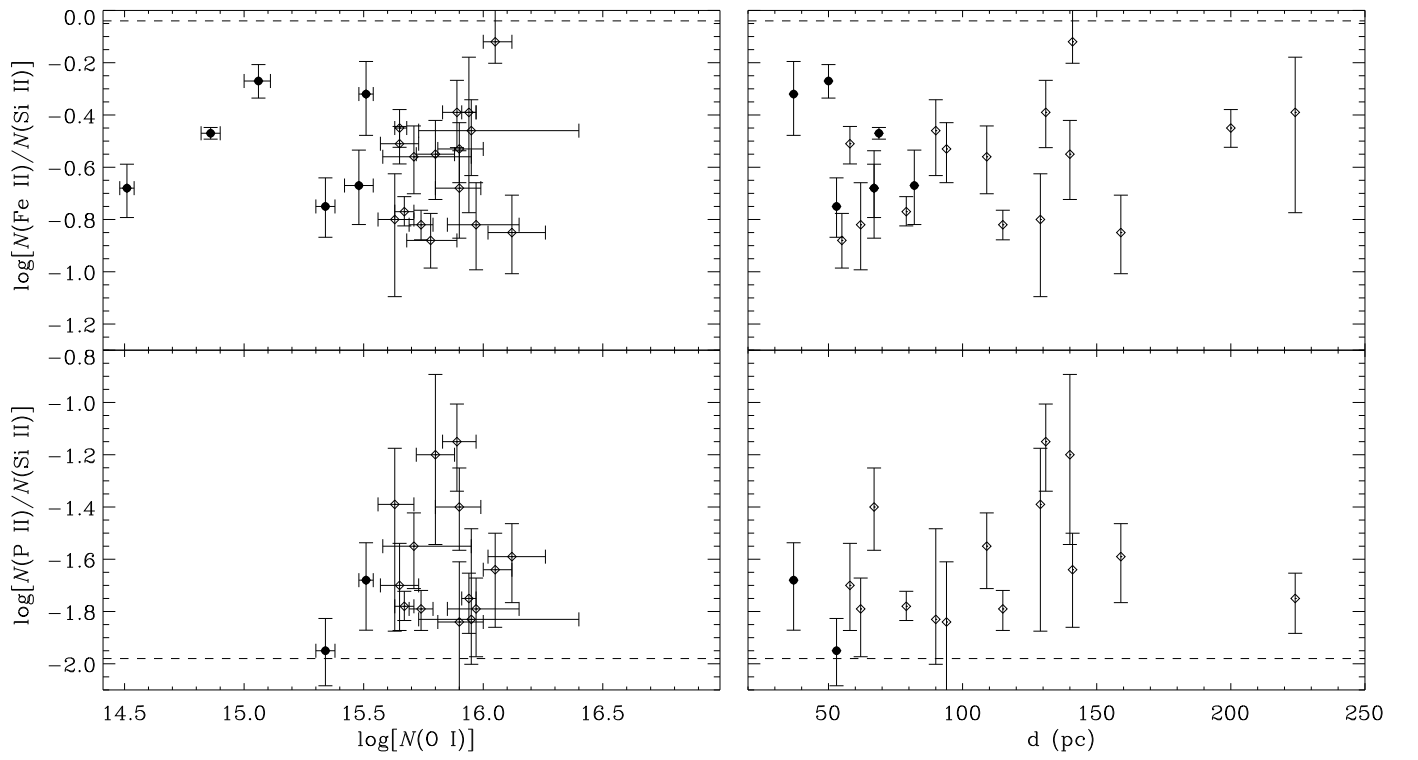


FIG. 7.— Logarithmic ratios of Fe II and P II to Si II against the total O I column density and against the distance of the sightlines. The dashed lines indicate the solar value of those ratios. The Local Bubble ($\log N(\text{O I}) \lesssim 15.60$) data points are shown with filled circles.

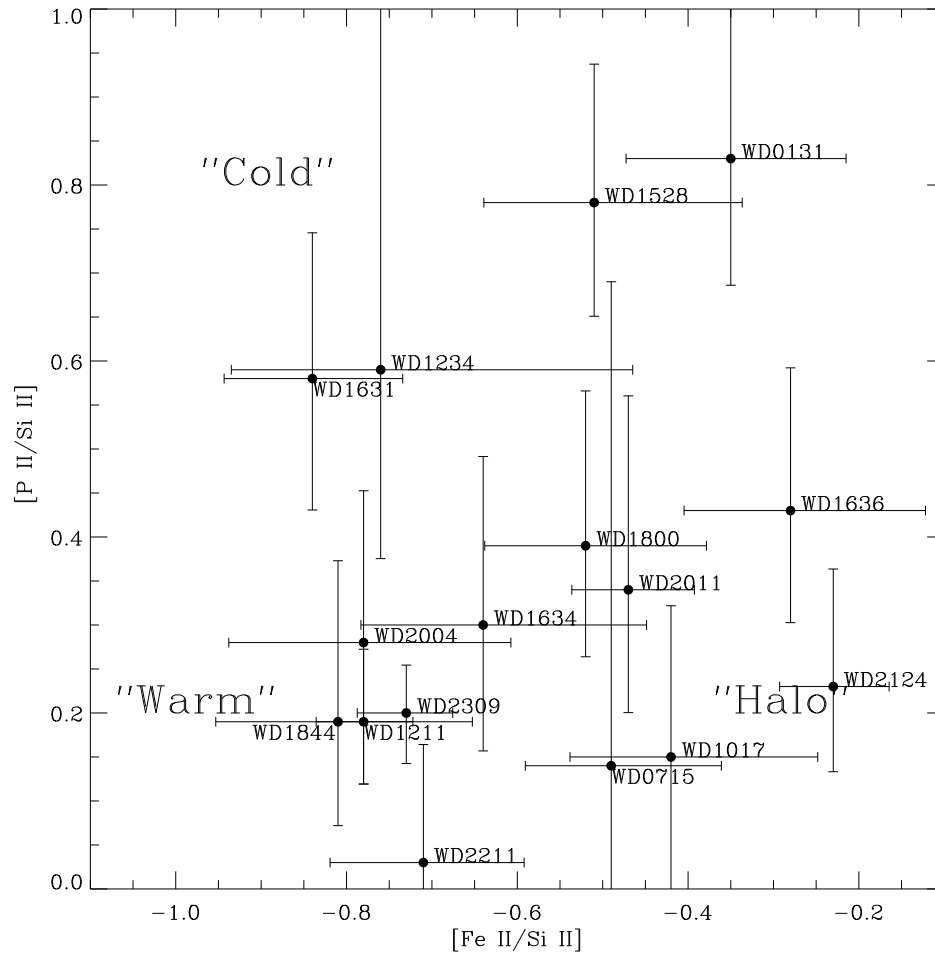


FIG. 8.— Logarithmic ratio of P II/Si II against Fe II/P II normalized to their solar values. The “Cold”, “Warm”, and “Halo” refer to depletion patterns observed in our Galaxy. We also indicate for each point the first 4 digits of the WD.

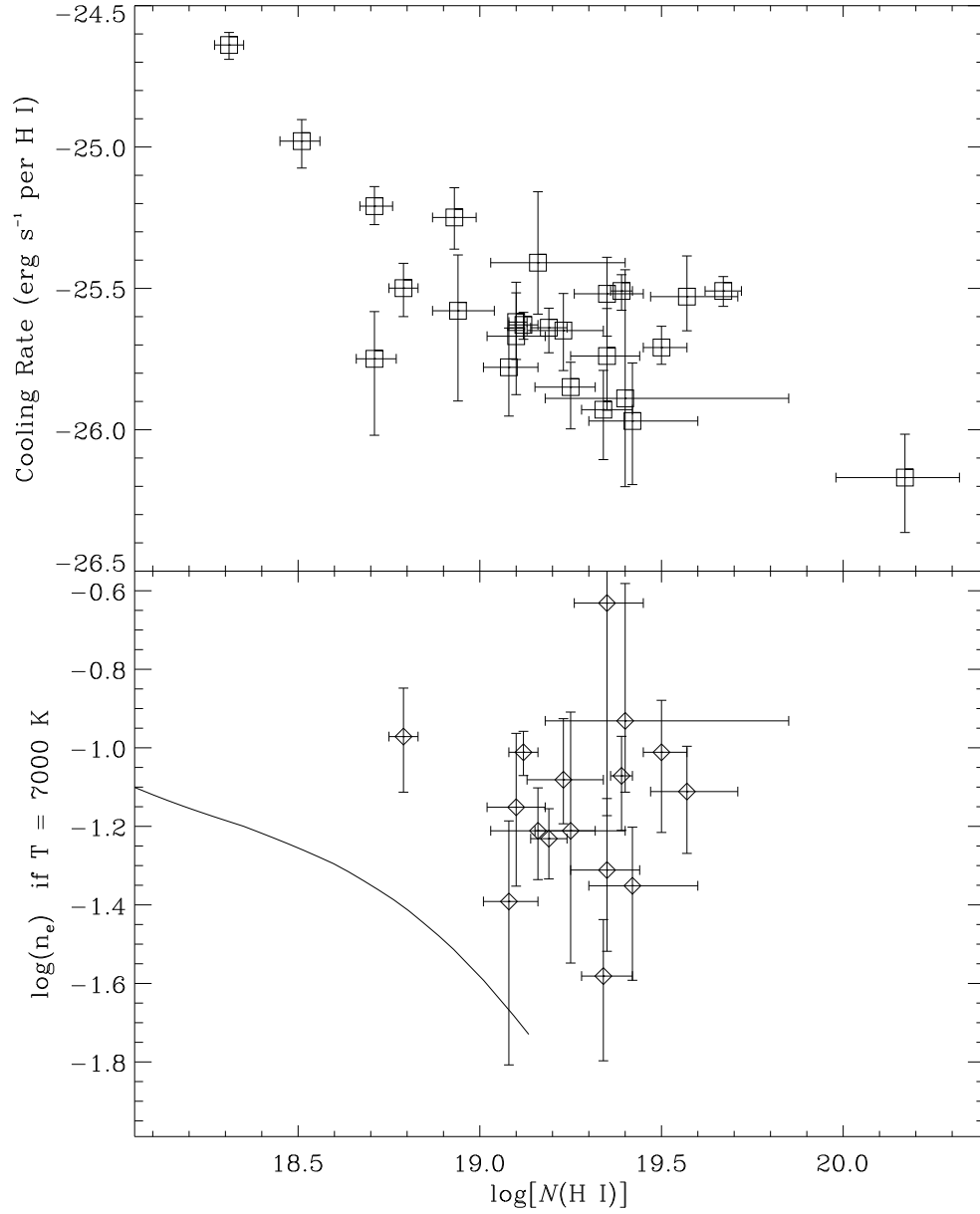


FIG. 9.— Logarithmic of the cooling rate in erg s^{-1} per H I atom (upper panel) and of the electron density in cm^{-3} (lower panel) against the total H I column density (the latter being derived from O I: $\log N(\text{H I}) = \log N(\text{O I}) + 3.5$) (see § 8 for more details). For clarity, we do not show the lower limits, but none contradicts the measured values. Also shown as a solid line is $\log n_e$ from Figure 6.